## Progress and perspectives of lithium aluminum germanium phosphate-based solid electrolytes for lithium batteries

Zhang, Yue; Liu, Hanshuo; Xie, Zhong; Qu, Wei; Freschi, Donald J.; Liu, Jian



**Publisher's version / Version de l'éditeur:**
https://doi.org/10.1002/adfm.202300973
*Advanced Functional Materials, 33, 32, 2023-04-28*

ADVANCED FUNCTIONAL MATERIALS
www.afm-journal.de



# Progress and Perspectives of Lithium Aluminum Germanium Phosphate-Based Solid Electrolytes for Lithium Batteries

*Yue Zhang, Hanshuo Liu, Zhong Xie, Wei Qu, Donald J. Freschi, and Jian Liu**

**Solid-state lithium batteries are considered promising energy storage devices due to their superior safety and higher energy density than conventional liquid electrolyte-based batteries. Lithium aluminum germanium phosphate (LAGP), with excellent stability in air and good ionic conductivity, has gained tremendous attention over the past decades. However, the poor interface compatibility with Li anode, slow Li-ion conduction in thick pellets, and high-temperature sintering procedure limit the further development of LAGP solid electrolytes in practical applications. This review comprehensively summarizes the crystal structure, Li-ion conducting mechanism, and various synthesis methods, especially the latest thin-film preparation approach. The underlying reason for Li/LAGP interfacial instability is identified, followed by several advanced interface engineering strategies, for example, introducing a functional interlayer. The integration design of LAGP-based solid electrolytes and cathode is also highlighted to enable high-loading cathodes. Additionally, recent progress of lithium-oxygen and lithium-sulfur batteries with LAGP-based solid electrolytes is discussed. Moreover, the different Li-ion migration pathways, preparation procedures, and electrochemical performance of polymer-LAGP composite solid electrolytes in Li-ion batteries are introduced. Lastly, the remaining challenges and opportunities are proposed to encourage more efforts in this field. This review aims to provide fundamental insights and promising directions toward practical LAGP-based solid-state batteries.**

## 1. Introduction

Lithium-ion batteries (LIBs) have been developing rapidly and widely applied in portable devices and clean transportation (e.g., electric vehicles) over the past decades due to their high energy/power density and cycle life.[1] Moreover, LIBs are promising devices for renewable solar/wind energy storage and conversion to achieve stable power output.[2] One main challenge for LIBs commercialization is the safety concern caused by the usage of flammable liquid electrolytes that have a risk of leakage or explosion during overcharge or abused operations.[3] Therefore, it is an urgent task to replace liquid electrolytes with solid-state electrolytes (SSEs) for the further development of LIBs. The use of SSEs also allows flexible cell configuration and simplifies cell packaging, thus enabling higher energy density.[4]

Ideal SSEs are expected to possess low cost, good processibility, high ionic conductivity comparable to that of liquid electrolytes, wide electrochemical stability window to match high-voltage cathodes, and excellent mechanical properties to resist lithium (Li) dendrites growth.[5] Moreover, excellent interfacial compatibility between SSEs and Li or cathode is desired to ensure continuous Li-ion conduction at the interface.[4b,6] Generally, SSEs can be classified into solid polymer electrolytes (SPEs), inorganic solid electrolytes (ISEs), and composite solid electrolytes (CSEs). SPEs, composed of polymer matrix and Li salts, are found to realize Li-ion transport by local relaxation and continuous segmentation rearrangement of the polymer chains.[7] SPEs have good flexibility and interfacial

Y. Zhang, J. Liu
School of Engineering
Faculty of Applied Science
University of British Columbia
3333 University Way, Kelowna, British Columbia V1V 1V7, Canada
E-mail: Jian.liu@ubc.ca

The ORCID identification number(s) for the author(s) of this article can be found under https://doi.org/10.1002/adfm.202300973.



DOI: 10.1002/adfm.202300973

Y. Zhang, J. Liu
Pacific Institute for Climate Solutions and School of Environmental Studies
University of British Columbia
Kelowna, British Columbia V1V 1V7, Canada
H. Liu, Z. Xie, W. Qu
National Research Council Canada
4250 Wesbrook Mall, Vancouver, British Columbia V6T 1W5, Canada
D. J. Freschi
Fenix Advanced Materials
2950 Highway Drive, Trail, British Columbia V1R 2T3, Canada

contact with Li anode or cathodes but low ionic conductivity ($<10^{-4}$ S $cm^{-1}$) at room temperature and limited oxidation stability (≈4 V).[8] In comparison, the fast Li-ion transport of ISEs can be achieved by defect sites of glassy or crystalline inorganics, while ISEs suffer from poor interfacial stability against Li metal and slow Li-ion conduction at solid–solid interfaces.[9] CSEs usually integrate the advantages of SPEs and ISEs and have enhanced ionic conductivity, wide electrochemical stability window, and interfacial stability against Li anode.[3,10]

ISEs play a critical role in facilitating Li-ion conduction and realizing a high energy density of a solid-state battery. To date, numerous ISEs have been extensively investigated, including garnet type,[11] sodium superionic conductor (NACISION) type,[5b,12] perovskite type,[13] anti-perovskite type,[14] and sulfide ISEs.[15] Among the various Li-ion conductors, $Li_{1.5}Al_{0.5}Ge_{1.5}(PO_4)_3$ (LAGP), a NASICON-type inorganic solid electrolyte, has attracted tremendous research efforts as promising ISEs over decades due to the high ionic conductivity and excellent stability against moisture.[16] There are three main challenges in LAGP-based solid-state batteries.[17] First, the total ionic conductivity of LAGP solid electrolytes (SEs) relies on the Li-ion conduction in crystalline grains and through grain boundaries.[18] Since the Li+ transfer is much slower at the grain boundary than inside the grain, it is essential to reduce the grain boundary resistance as it determines the overall resistance of the solid-state cell.[19] It is found that LAGP grain size and the ionic conductivity at grain boundaries can be adjusted by controlling crystalline temperature,[20] the content of $Al_2O_3$,[21] the proper addition of LiF[16a] or $B_2O_3$,[22] etc. Second, a chemically formed interphase with mixed ionic and electric conductivity was generated at the Li/LAGP interface caused by the Ge reduction reaction.[23] This interphase can lead to increased cell resistance, the fracture of LAGP, and ultimate failure, especially with an applied current.[24] Third, the large thickness of LAGP pellets (>200 μm) offsets the advantages of high-energy-density batteries. The thinner SEs can accomplish higher gravimetric/volumetric energy density but are prone to internal short circuits resulting from Li dendrite penetration.[4a] It is vital to have a thin LAGP that enables both high energy density and mechanical properties. To date, there are few articles that summarize the progress and prospects of LAGP-based all-solid-state lithium batteries.

From the above perspectives, this paper aims to provide a systematic review of progress, advances, and inspirations for the preparation and application of LAGP in solid-state batteries. The first section summarizes the crystal structure and Li-ion conducting mechanism, and various fabrication methods. In particular, the effect of the thickness of solid electrolytes on cell energy density is introduced, followed by the latest methodology of thin-film solid electrolytes (<50 μm). In the next section, the challenging Li/LAGP failure mechanism and LAGP/electrode (LAGP/Li or LAGP/cathode) interface interfacial engineering design are presented. The structure design of semi-solid-state LAGP-based batteries is also discussed. Then, the promising LAGP/polymer composite solid electrolytes are summarized. Lastly, we provide a summary of current challenges and promising structure design strategies for a better understanding and further development of LAGP-based solid-state batteries.

## 2. LAGP Structure, Li-Ion Conducting Mechanism, and Synthesis

### 2.1. LAGP Structure and Li-Ion Conducting Mechanism

NASICON-type LAGP ($Li_{1+x}Al_xGe_{2-x}(PO_4)_3$) has the main phase of $LiGe_2(PO_4)_3$ and partial replacement of $Ge^{4+}$ by $Al^{3+}$ ions, as shown in **Figure 1**a. In the crystal structure of $LiGe_2(PO_4)_3$, Li-ions are stable at the interstitial sites between $GeO_6$ octahedrons, and $GeO_6$ and $PO_4$ are linked by corner-sharing to build a 3D skeleton for Li-ions diffusion. After the partial substitution of $Ge^{4+}$ by $Al^{3+}$ ions, additional Li-ions are introduced to charge-balance the substitution defect and increase $Li^+$ charge carrier concentration.[25] Heat treatment temperature is critical in determining the internal structure of LAGP in solid-state synthesis[18a] or sol–gel approach.[26] Pershina et al.[27] studied the effect of crystallization temperature on phase composition and ionic conductivity of LAGP SEs. Impurity phase $GeO_2$ was also observed at the crystalline temperature above 750 °C. To understand the Li-ion conductivity of LAGP-type SSEs, researchers studied the Li-ion diffusion mechanism inside LAGP. Previous studies reported that Li-ions were mainly allocated at the 6b site, and excess Li caused by aliovalent substitution resided at 18e sites.[28] The energy potential of $Li^+$ was smoothened by increasing interstitial $Li^+$ and enhancing the connection between available sites and mobile ions (Figure 1b). Hayamizu et al.[29] studied the long-range Li-ion diffusion in LAGP by $^7$Li pulsed-gradient spin-echo NMR. Han et al.[30] used integrated first-principle density functional theory (DFT) to calculate energies for different configurations of four pairs of Li in LAGP at the sites of (6b, 18e), (6b, 36f), (18e, 36f), and (36f, 36f). As presented in Figure 1c, two 36f sites with a mutual distance of 3.29 Å in LAGP were more thermodynamically stable instead of one 6b and one 18e site. Figure 1d shows the $Li^+$ diffusion mechanism in $Li_{1.5}Al_{0.5}Ge_{1.5}(PO_4)_3$ at 800 K by molecular dynamics (MD) simulations. $Li^+$ oscillation at M1 or M2 offered $Li^+$ hopping energy to the next 36f site, and fast $Li^+$ exchange was achieved by the back-and-forth oscillation.[25]

### 2.2. Synthesis Methods and Modification

Generally, LAGP can be synthesized by either solid-based approaches, such as solid-state synthesis, melt-quenching, fast sintering, hot-pressing, or liquid-based methods, including sol–gel and co-precipitation. Additionally, there is a growing interest and effort in developing thin-film LAGP. **Table 1** summarizes the ionic conductivity, activation energy, relative density, and grain size of LAGP prepared from solid or liquid-based methods.

#### *2.2.1. Solid-State Synthesis*

Solid-state synthesis is a traditional method for the preparation of LAGP pellets. Precursors ($Al_2O_3$, $GeO_2$, $Li_2CO_3$, and $(NH_4)_2HPO_4$) are fully mixed and ground by ball-milling and then calcined at high temperature for a solid-state reaction ($0.75Li_2CO_3 + 1.5GeO_2 + 3NH_4H_2PO_4 + 0.25Al_2O_3 \rightarrow Li_{1.5}Al_{0.5}Ge_{1.5}PO_4 + 3NH_3\uparrow + 0.75CO_2\uparrow + 4.5H_2O\uparrow$).

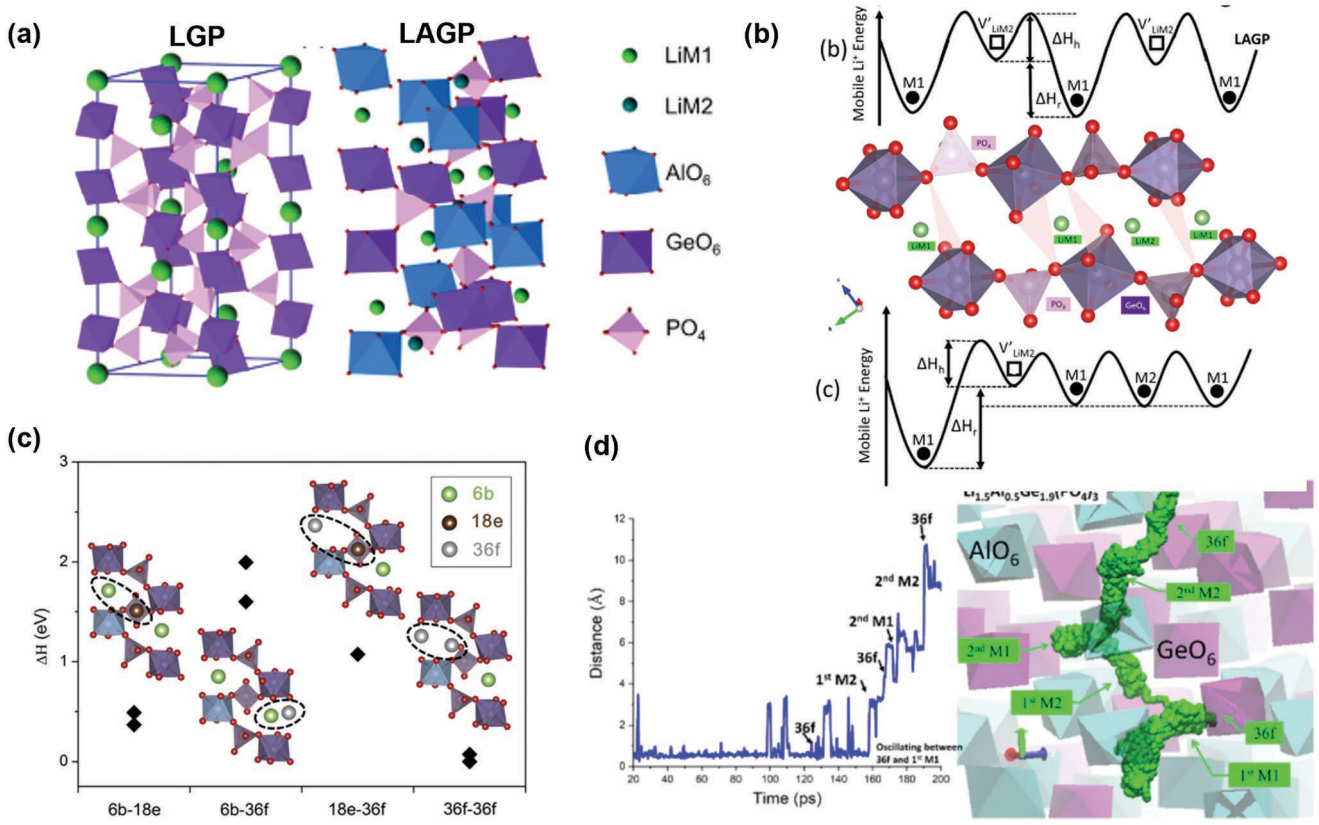


**Figure 1.** a) Crystal structure of LAGP. b) Schematic diffusion pathway and variation of $Li^+$ potential with the corresponding position in LAGP crystal with an empty M2 site or M2 site sufficiently filled. Reproduced with permission.[25] Copyright 2019, American Chemical Society. c) DFT calculated energies for different configurations of four pairs of Li in LAGP. Reproduced with permission.[30] Copyright 2015, Elsevier B. d) $Li^+$ conducting pathways in $Li_{1.5}Al_{0.5}Ge_{1.5}(PO_4)_3$ at 800 K. Reproduced with permission.[25] Copyright 2019, American Chemical Society.

After being cooled down to room temperature, the as-obtained pellet usually possesses a crystalline structure, compact surface, high ionic conductivity, and density. However, high sintering temperatures might cause lithium loss and induce the formation of a secondary phase,[31] thus increasing the grain boundary barrier for Li-ion transport.

In the melt-quenching method, precursors are first melted at a higher temperature (>1000 °C) and quenched to room temperature. The as-obtained amorphous glass is subsequently sintered as LAGP glass ceramics. Kun et al.[21] studied the crystal identification and microstructure of $Li_{1+x}Al_xGe_{2-x}(PO_4)_3$ glass-ceramics with various $Al_2O_3$ addition, and the highest ionic conductivity of $5.8 \times 10^{-4}$ S $cm^{-1}$ was reached in $Li_{1.5}Al_{0.5}Ge_{1.5}(PO_4)_3$ with $LiGe_2(PO_4)_3$ main phase and $AlPO_4$ impurity phase. Excess $Al_2O_3$ addition caused the formation of larger crystallites and impurities ($Li_4P_2O_7$, $AlPO_4$, $GeO_2$) and decreased Li-ion transference number.[32] Glass crystallization temperature is a critical parameter in controlling grain growth and Li-ion transportation at grain boundary.[18b] Pershina et al.[27] determined the optimal crystallization temperature 820 °C and found that a higher crystallization temperature (850 °C) led to the formation of microcracks and voids, which increased the barrier for grain-grain contact, decreased electrolyte density, and eventually reduced Li-ion grain-boundary ionic conductivity.

Spark plasma sintering (SPS) and microwave sintering are fast sintering processes to ensure intimate solid-solid LAGP particle interfaces.[33] LAGP powder is loaded in an electrically conductive die under pressure. A pulsed current is applied to pass through the powder and generate localized high temperatures at particle interfaces due to Joule heating.[34] High pressure and localized temperature melt grain boundary, increase particle densification, and facilitate Li-ion diffusion at the interface.[35] More importantly, SPS can be completed in a short period (10 min) at a lower temperature (600 °C) than traditional solid-state synthesis or melt-quenching method. High SPS temperature accelerated the growth of crystallite size and reduced inter-/intraparticle grain boundary.[36]

LAGP synthesized by the hot-pressing technique also possessed comparable total ionic conductivity ($1.8 \times 10^{-4}$ S $cm^{-1}$), and this sintering process requires a lower sintering temperature (550 °C) and holding time (30 min) than conventional sintering process.[37] A higher hot-pressing temperature of 750 °C resulted in the formation of impurity phases ($AlPO_4$, metallic Ge) by the partial decomposition of LAGP, and as-sintered LAGP pellets were fragile and difficult for cell assembly.[38] Lu et al.[39] prepared amorphous LAGP by melt-quenching method and then remodeled it into the partially crystallized structure by the hot-press technique. Zhu et al.[40] improved the Li-ion diffusion at the grain boundary by hot-pressing the LAGP powder obtained by the sol–gel method.

**Table 1.** Summary of different synthesis methods and properties of LAGP pallets.

| Electrolyte | Synthesis method | Thickness [mm] | $\sigma_{25\ °C,\ total}$ [S cm$^{-1}$] | Activation energy $E_a$ [eV] | Relative density [%] | Grain size [μm] | Ref. |
|---|---|---|---|---|---|---|---|
| $Li_{1.5}Al_{0.5}Ge_{1.5}(PO_4)_3$ | Cold sintering | — | $5.4 \times 10^{-5}$ | $0.40 \pm 0.01$ | 75.0 | — | [45] |
| $Li_{1.5}Al_{0.5}Ge_{1.5}(PO_4)_3$ | Hot-pressing | — | $3 \times 10^{-4}$ | 0.41 | ≥99.0 | — | [38] |
| $Li_{1.5}Al_{0.5}Ge_{1.5}(PO_4)_3$ | Hot-pressing | — | $1.8 \times 10^{-4}$ | - | — | — | [37] |
| $Li_{1.5}Al_{0.5}Ge_{1.5}(PO_4)_3$ | Sol–gel | 1 | $4.18 \times 10^{-4}$ | 0.30 | — | 0.2–1 | [42] |
| $Li_{1.5}Al_{0.5}Ge_{1.5}(PO_4)_3$ | Sol–gel | — | $3.1 \times 10^{-4}$ (30 °C) | 0.37 | 76 | 1–2 | [41] |
| $Li_{1.4}Al_{0.4}Ge_{1.6}(PO_4)_3$ | Sol–gel | 2 | $1.22 \times 10^{-3}$ | 31.1 kJ mol$^{-1}$ | 88 | — | [20] |
| $Li_{1.5}Al_{0.5}Ge_{1.5}(PO_4)_3$ | Sol–gel and hot-pressing | 1 | $2.7 \times 10^{-4}$ | 0.31 | — | — | [40] |
| $Li_{1.5}Al_{0.5}Ge_{1.5}(PO_4)_3$ | Sol–gel | 1 | $1.8 \times 10^{-4}$ | — | — | | [26] |
| $Li_{1.5}Al_{0.5}Ge_{1.5}(PO_4)_3$ | Melt-quench | 0.8 | $1.64 \times 10^{-4}$ | 0.30 | 99.6 | 2–4 | [39] |
| $Li_{1.5}Al_{0.4}Ga_{0.1}Ge1._5(PO_4)_3$ | Microwave sintering | — | $1.64 \times 10^{-4}$ (bulk) | 0.66 | — | — | [33b] |
| $Li_{1.5}Al_{0.5}Ge_{1.5}(PO_4)_3$ | High-frequency microwave processing | — | $2.77 \times 10^{-4}$ | 0.327 | — | 0.3–0.9 | [33a] |
| $Li_{1.5}Al_{0.5}Ge_{1.5}(PO_4)_3$ | Spark plasma sintering | — | $3.29 \times 10^{-4}$ | 0.239 | 97.6 | 0.4–0.8 | [35] |
| $Li_{1.5}Al_{0.5}Ge_{1.5}(PO_4)_3$ | Spark plasma sintering | — | $1.33 \times 10^{-4}$ (20 °C) | 0.38 | 97 | 0.7 | [61] |
| $Li_{1.5}Al_{0.5}Ge_{1.5}(PO_4)_3$ | Radio frequency sputtering | 0.0012 | $1.29 \times 10^{-6}$ | 0.25 | — | 1 | [62] |
| $Li_{1.5}Al_{0.5}Ge_{1.5}(PO_4)_3$ | Co-precipitation | — | $7.8 \times 10^{-5}$ | — | 97 | 1 | [43] |
| $Li_{1.5}Al_{0.5}Ge_{1.5}(PO_4)_3$ | Melt-spun and annealing | — | $8.8 \times 10^{-3}$ | | — | 0.05-0.2, fibers | [63] |
| $Li_{1.5}Al_{0.5}Ge_{1.5}(PO_4)_3$ | Annealing and nano-polishing | 1 | $3.9 \times 10^{-4}$ | — | — | — | [46] |
| $Li_{1.4}Al_{0.4}Ge_{1.6}(PO_4)_3$ | Tape casting | 0.075 | $3.38 \times 10^{-4}$ | 30.57 kJ mol$^{-1}$ | 88 | — | [55] |
| $Li_{1.5}Al_{0.5}Ge_{1.5}(PO_4)_3$ | Aerosol deposition | 0.010 | $5 \times 10^{-6}$ | — | 80 | 0.1 | [56] |
| $Li_{1.5}Al_{0.5}Ge_{1.5}(PO_4)_3$ | Solution process | 0.070 | $2 \times 10^{-5}$ | — | 80 | — | [64] |
| LAGP thin film | Hot-pressing | 0.060 | $1 \times 10^{-3}$ (80 °C) | 16.62 kJ mol$^{-1}$ | — | — | [16b] |
| N-doped LAGP film | Magnetron sputtering | 0.001 | $2.3 \times 10^{-4}$ (20 °C) | 0.374 | — | — | [57] |
| LAGP-$Ba_{0.6}Sr_{0.4}TiO_3$ | Sintering | — | $5.08 \times 10^{-3}$ (27 °C) | 31.8 kJ mol$^{-1}$ | 3.26 g cm$^{-3}$ | 0.43–3 | [51] |
| LAGP-$B_2O_3$ | Melt-quenching | — | $6.9 \times 10^{-4}$ | 21.6 kJ mol$^{-1}$ | — | 0.8–1.5 | [22] |
| LAGP-$B_2O_3$- $Bi_2O_3$ | Sol–gel | 1 | $3.4 \times 10^{-4}$ | — | 93.4 | 0.056 | [47] |
| LAGP/SBA-15 | Balling and sintering | — | $1 \times 10^{-5}$ | — | — | <0.6 | [48] |
| Mg-doped LAGP | Balling and sintering | — | $5.16 \times 10^{-4}$ | 0.275 | 95 | — | [49] |
| LAGP-LLTO | Balling and sintering | — | $4.04 \times 10^{-4}$ | 0.37 | — | — | [50] |
| LAGP-LiF | Melt-quenching | — | $3.17 \times 10^{-4}$ | 0.31 | 97.7 | 0.155 | [16a] |

### *2.2.2. Liquid-Based Method*

The sol–gel method provides a facile route to prepare pure LAGP powder due to lower heat treatment temperature and time.[41] Solvents are required to mix with precursors and form a colloid solution, which is heated until a gel network occurs. Subsequently, the dried gel is reground, die-pressed into pellets, and sintered for crystallization. Germanium precursor sources,[42] solvents (citric acid and ethylene glycol),[20,40] and crystallization temperature and time[26] play an essential role in determining crystallite structure and Li-ion conductivity. Liu et al.[42] synthesized LAGP powder by a sol–gel method with inorganic $GeO_2$ precursor as a replacement for costly organic germanium compounds ($Ge(OCH_3)_4$ or $Ge(OC_2H_5)_4$). The as-prepared LAGP pellets have irregular shapes over a range of 0.2–1 μm and high bulk and total ionic conductivities of $7.76 \times 10^{-4}$ and $4.18 \times 10^{-4}$ S cm$^{-1}$, respectively.

Kotobuki[43] synthesized LAGP powder through a co-precipitation approach consisting of a ball-milling and sintering process at 650–900 °C. The crystallinity of the LAGP pellet increased versus the crystallization temperature. However, impurities were prominently observed at 850 and 900 °C, and pores were also found at the high sintering temperatures. Moreover, Janek et al.[44] reported an aqueous solution-based method for the preparation of LAGP and observed the increase of unit cell dimensions with lithium content for $Li_{1.5}Al_{0.5}Ge_{1.5}(PO_4)_3$ from neutron and synchrotron diffraction data. Berbano et al.[45] prepared LAGP by a cold sintering process (<200 °C), which employed a transient solvent (deionized water or ethanol) to assist densification. The mixture was then pressed under 400 MPa with a multistage non-equilibrium heating process at 25–160 °C for 20 min, followed by a 5-min crystallization at 650 °C. More investigations are required to find out the optimal

solvent and understand the Li-ion transport mechanism details during cold sintering process.

#### 2.2.3. Modification Approach

Zhou et al.[46] reported an ultra-smooth surface of LAGP by a simple nano-polishing approach to avoid pores or voids and enable intimate contact between LAGP and Li metal anode. The surface rough remarkably dropped to 30 nm after being polished using nanoscale sandpaper (50-30075 Allied USA). The grain-boundary ionic conductivity of LAGP can be enhanced by adding excess Li, as indicated by lower activation energy.[31] Park et al.[22] doped a sintering aid $B_2O_3$ into LAGP with a flat 6-numbered ring structure formed of boron and oxygen. The small amount of $B_2O_3$ decreased the crystallization temperature of LAGP pellets and increased the total ionic conductivity of LAGP. Structural modifiers such as $B_2O_3$ and $Bi_2O_3$,[47] mesoporous silica scaffolds,[48] or other dopants (Mg,[49] perovskite $Li_{0.348}La_{0.55}TiO_3$ particles,[50] $Ba_{0.6}Sr_{0.4}TiO_3$[51]) have been added to improve lithium-ion transport of LAGP. Lv et al.[16a] added 0.5 wt% low-volatile LiF in LAGP precursors to synthesize LAGP by a melt-quenching method, which lowered the crystallization temperature from 622 to 605 °C, increased Li-ion concentration to decrease the activation energy and promote Li-ion conduction at the grain boundary. Gomez et al.[52] developed ceramic-salt LAGP-LiTFSI composite electrolytes by cold sintering at 130 °C. The as-obtained LAGP-LiTFSI composites possessed comparable relative density above 90% and 10–4 S $cm^{-1}$ to LAGP pellets by sintering above 800 °C.

#### 2.2.4. Thin-Film Preparation

As mentioned above, conventional oxide LAGP SEs have the advantages of high ionic conductivity, good mechanical strength, oxidation, and moisture stability. However, the thickness of LAGP pallets is usually ≈1 mm in early studies, as listed in Table 1, which increases the internal resistance of ASSLBs and drags down the overall gravimetric/volumetric energy density. More importantly, the rising materials and manufacturing costs offset the desirable high energy density of ASSLBs. The cost estimation from Rupp et al.[53] suggests that the cost of solid electrolytes has to be controlled under US$4 $m^{-2}$ in order to meet the US Department of Energy cost target (US$10–12 $m^{-2}$) for the cell repeat layers of a solid-state battery, given that the optimistic estimating costs of US$7 $m^{-2}$ and US$1 $m^{-2}$ for cathode and 20-µm Li metal sheet, as shown in **Figure 2**a. However, conventional ceramic processing requires high-temperature sintering from 100 to 1000 °C, and the as-processed ceramic pellets have a large thickness range from 300 µm to 1 mm, as summarized in Figure 2b. The dependence of energy density for all-solid-state lithium-ion pouch cells on SE thickness has been revealed by Wang et al.[54] and illustrated in Figures 2c and 2d. To achieve the high energy densities of 300 and 400 Wh $kg^{-1}$ for Li/LFP and LI/NCM811 cells, the thickness of LAGP film should be less than 36 µm and 40 µm, respectively. Therefore, it is essential to develop LAGP thin film fabrication techniques to reduce processing cost and accomplish high energy density.

Tape casting,[55] aerosol deposition,[56] magnetron sputtering,[57] and hot-pressing[16b] have been reported to enable ultrathin LAGP films ranging from 10 to 75 µm. The preparation process for $Li_{0.34}La_{0.56}TiO_3$ (LLTO) film by tape casting method[54] is presented in Figure 2e. The LLTO slurry was cast on polyethylene terephthalate (PET) release film serving as mechanical support. The thickness of the casting film can be controlled by a height-adjustable scraper. The 62-µm was stripped off from PET film after solvent volatilization. In addition, polymer-in-ceramic solid electrolytes are another effective strategy to integrate wide advantages of ionic conductivity, flexibility, mechanical properties, electrochemical stability, and thermal stability from polymer and ceramic solid electrolytes alone.[58] Yao et al.[59] developed a 20-µm 3D polymer-ceramic solid electrolyte film consisting of LLZTO, LiTFSI, DETA, PEGDE, and PEGDME by grinding, two-step heat curing, and pressing procedures, as seen in Figure 2f,g. This film possessed 90 wt% LLZTO content and a robust Li-ion polymeric network, thus leading to an outstanding ionic conductance of 41.21 mS at 30 °C. The 3D network also contributed to mechanical strength and flexibility. Wu et al.[60] prepared a PEGMA-LAGP-Li solid electrolyte/lithium integration structure by in situ copolymerization onto Li foil through a thermal-initiated free-radical reaction (Figure 2h). In comparison with ex situ formed PEGMA-LAGP/Li configuration, this integration structure ensured superior interfacial compatibility between PEGMA-LAGP and Li anode (>3500 h cycles in symmetrical cells) and better rigidity (3 GPa Young's modulus) against Li dendrite growth (Figure 2i), with the record-breaking thickness of 8.5 µm. Accordingly, structure design and thin-film manufacturing are critical in achieving a high energy density of ASSLBs, which requires more cost-effective approaches to reducing processibility costs.

## 3. Interface Engineering Design in LAGP-Based All-Solid-State Batteries

### 3.1. Failure Mechanism at the Li/LAGP Interface

The further development of LAGP in practical battery applications suffers from the poor chemical stability of LAGP against Li metal and large thickness (200 µm to 1 mm). Amine et al.[64] prepared a self-standing LAGP thin film with a small thickness of only 70 µm using a solution-based process. As illustrated in **Figure 3**a, LAGP particles were first mixed with PVDF-HFP polymer and DMF/THF solvent, and the solution was cast onto a polypropylene sheet followed by a 10-h sintering process at 850 °C. The as-sintered LAGP film had a lower relative density (80%) than standard 1-mm LAGP pellets (≈95%) prepared by conventional solution-free methods. The as-obtained LAGP thin film also possessed a high ionic conductivity of $2 \times 10^{-5}$ S $cm^{-1}$ at 25 °C and a low electronic conductivity value of $1.1 \times 10^{-9}$ S $cm^{-1}$. After cycling at 25 and 80 °C, Li–Ge alloy was formed at the Li/LAGP interface as investigated by synchrotron high energy X-ray Diffraction (HEXRD) spectra (Figure 3b). An anisotropic volume change (lattice *a* increase and lattice *c* decrease) was found in the crystal structure of LAGP electrolyte, and the larger lattice parameter evolution at

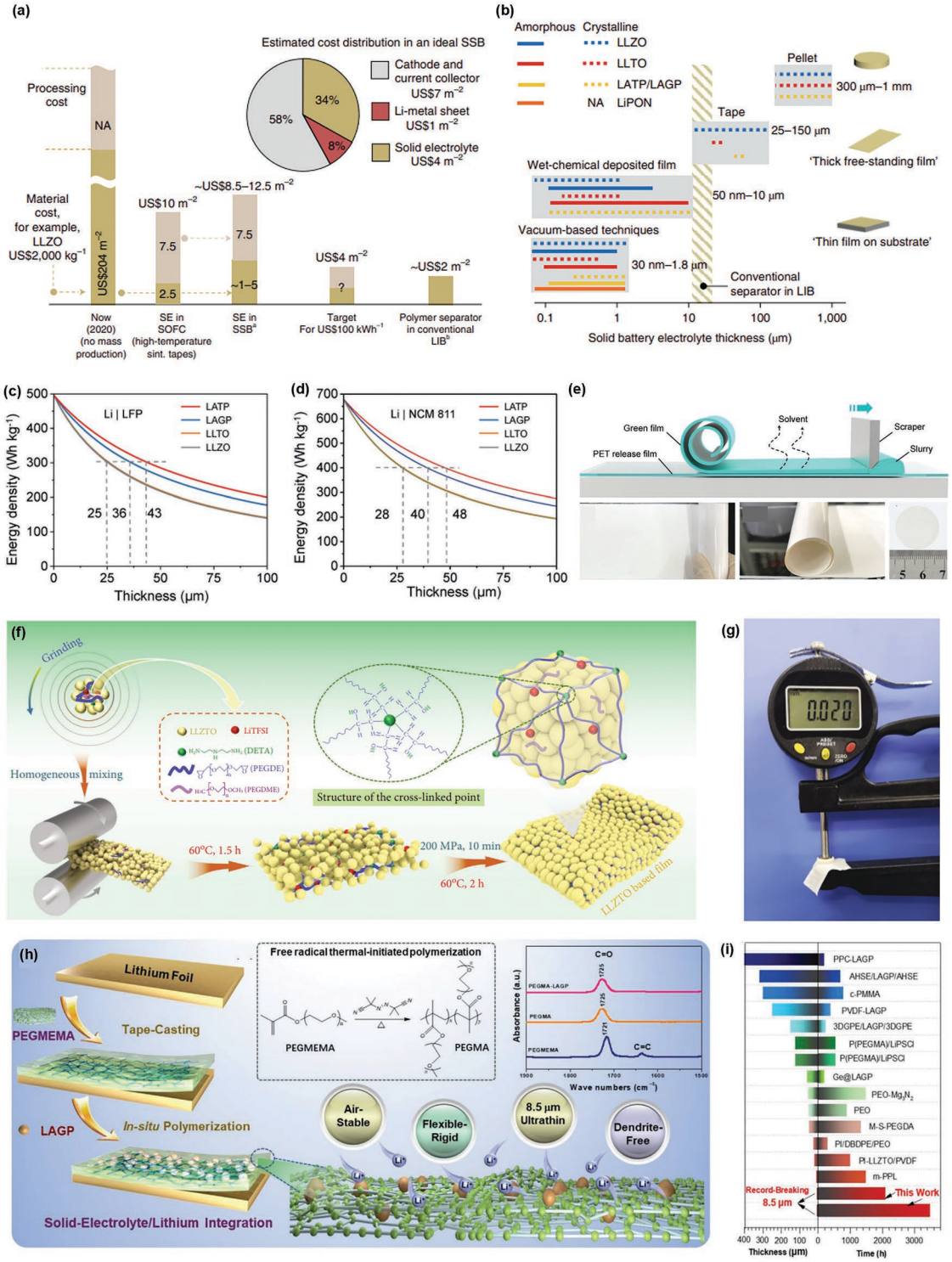


**Figure 2.** a) Estimated cost projection for an SSB to be competitive with a LIB based on LLZO estimations and material costs. b) Typical thickness ranges of solid-state electrolytes pellets, tapes, wet-chemical and vacuum-based deposited films. Reproduced with permission.[53] Copyright 2021, Springer Nature. Gravimetric energy density as a function of the thickness of several oxide ceramic thin-film electrolytes employing c) LFP and d) NCM cathode. e) Schematic for preparation and photographs of LLTO film using the tape-casting method. Reproduced with permission.[54] Copyright 2019, Wiley-VCH GmbH. f) Schematic illustration of synthesis procedure for ultrathin LLZTO-based solid electrolyte, g) photographs of LLZTO-based film. Reproduced with permission.[59] Copyright 2022, Beijing Institute of Technology Press Co., Ltd. h) Scheme of the synthetic process for in situ formation of PEGMA-LAGP-lithium, i) comparison of the cycling stability of Li|Li symmetric cells based on the thinnest in situ PEGMA-LAGP solid electrolyte and SSEs reported elsewhere. Reproduced with permission.[60] Copyright 2022, Wiley-VCH GmbH.

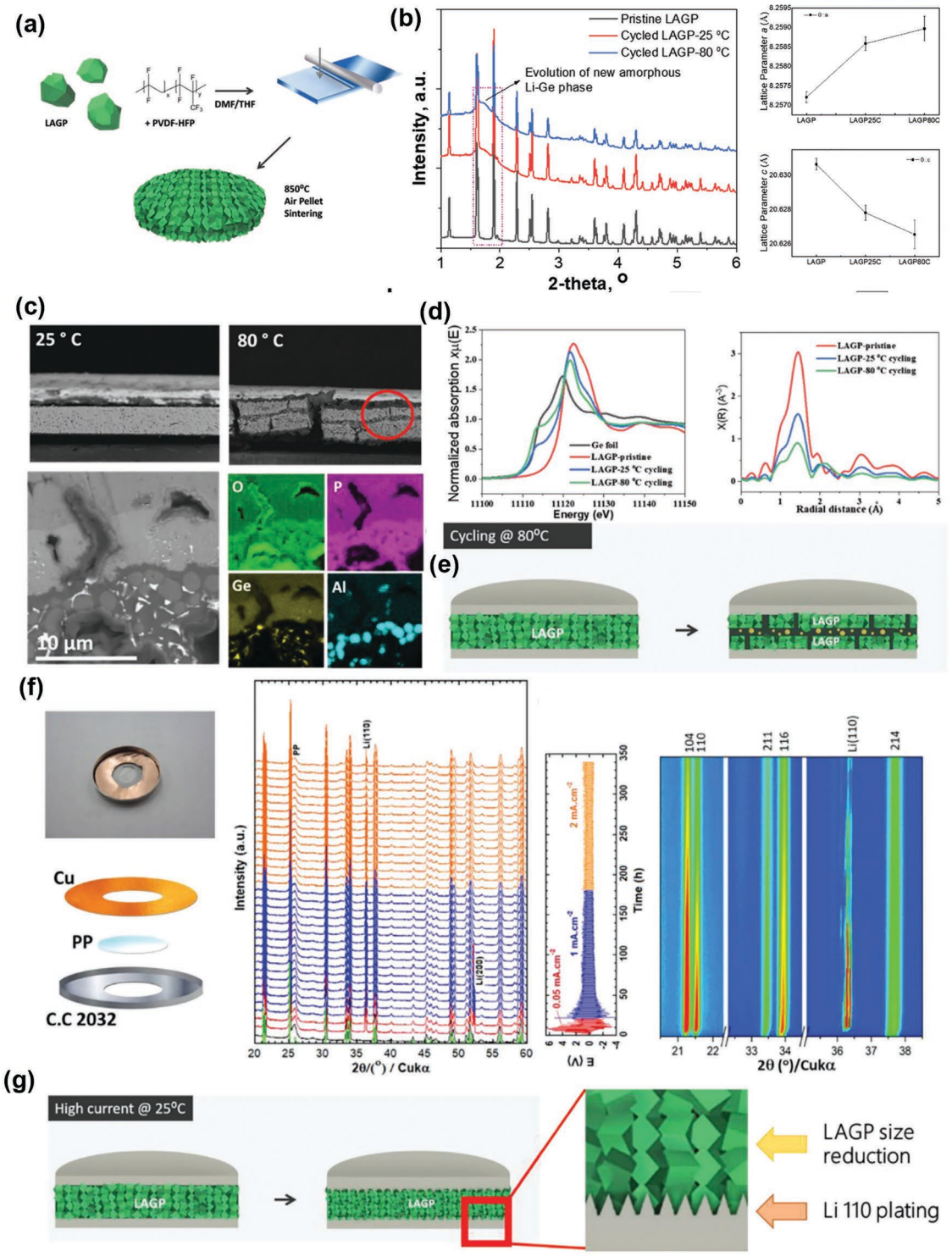


**Figure 3.** Li/LAGP interface investigation. a) Schematic illustration of LAGP pellet preparation, b) post-mortem synchrotron XRD patterns and lattice parameters of cycled LAGP at 25 and 80 °C, c) SEM and EDS mapping of the cycled LAGPs at 25 and 80 °C, d) Ge K-edge XANES spectra of LAGPs and Fourier transformed EXAFS spectra, e) scheme of decomposition reaction for the cycled LAGP at 80 °C, f) in situ XRD patterns of Li//LAGP sheet// Li and corresponding variation of voltage versus time, and contour plot of enlarged $2\theta$ ranges showing the up-shift of $2\theta$ and texturing of Li(110), and g) reaction of Li(110) alignment. Reproduced with permission.[64] Copyright 2020, Wiley-VCH GmbH.

80 °C implied the accelerated side reaction at high temperature. Furthermore, the cross-section of LAGP film cycled at 80 °C showed a Ge-rich degradation layer and agglomeration of Al/P-rich big particles, as presented in Figure 3c. Ge K-edge

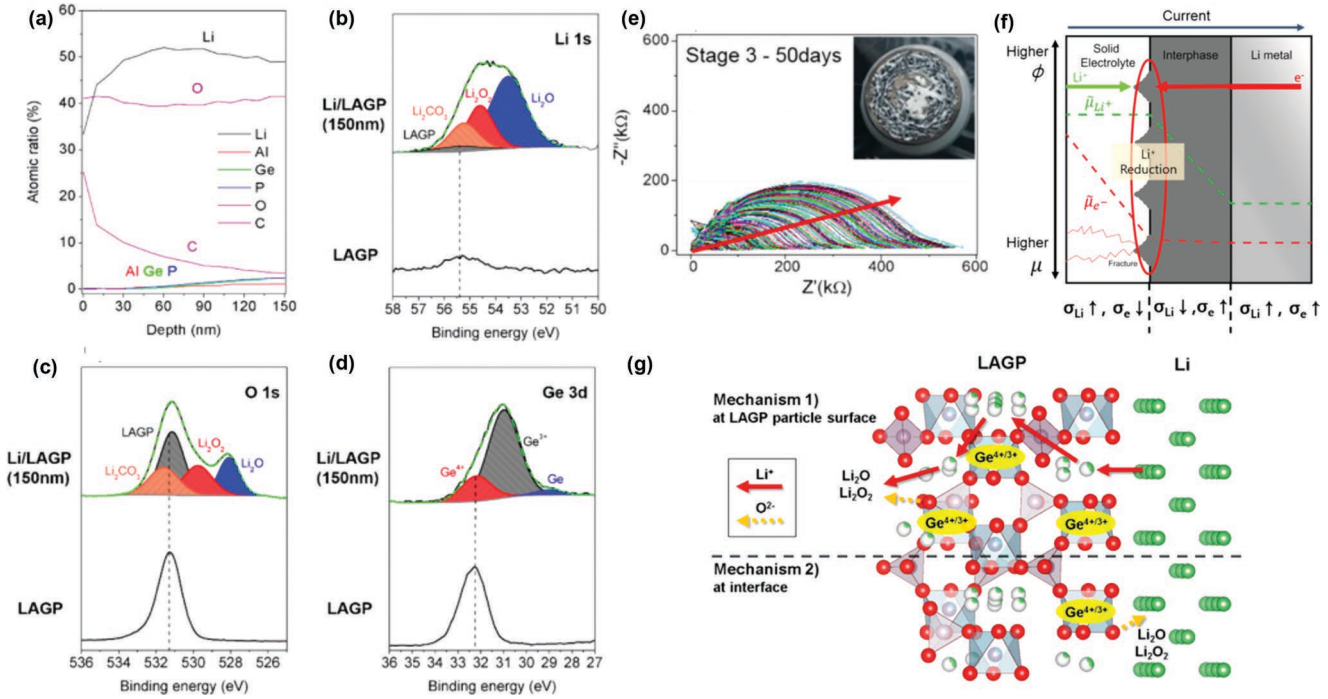


**Figure 4.** a) Depth profiling of Li/LAGP interface after detaching Li metal and b) Li 1s, c) O 1s, and d) Ge 3d XPS spectra. e) Nyquist plot of a Li/LAGP/Li cell over 50 days. f) Chemical potential change for Li-ions and electrons during electrochemical reactions. g) Interphase-forming mechanisms for Li metal and LAGP. Reproduced with permission.[24] Copyright 2017, American Chemical Society.

X-ray near-edge absorption spectroscopy (XANES) suggested a significantly decreased peak intensity and energy shift for cycled LAGPs (Figure 3d). The peak decrease in extended X-ray absorption fine structure might originate from the breakdown of LAGP crystalline size or loss of its crystallinity. Therefore, Ge reduction at Li/LAGP interface occurred to form an amorphous Li-Ge phase, and this process was more severe at a higher temperature. Upon cycling at 80 °C, Ge was also progressively reduced through the pellet cracks from both sides and ultimately generated a Ge-rich layer in the center of LAGP (Figure 3e). On the other hand, the collected in situ XRD data of Li/LAGP/Li cell (Figure 3f) showed peak intensity decrease, peak broadening, and peak up-shift, revealing a reduced crystallite size of LAGP and lattice parameter shortening. Li metal growth followed a preferential orientation along the (110) crystal face (Figure 3g) due to the intrinsic feature of lithium-ion electro-migration during the nucleation and growth.[65]

Kang et al.[24] conducted Li/LAGP interphase analysis by monitoring elemental depth distribution and XPS spectra (Li, Ge, O) on the surface of cycled LAGP (**Figure 4**a–d). The atomic ratios of Al/Ge/P were smaller than 1% on the surface, which had a minor increase with $Ar^+$-ion etching from the top down to 150 nm. O-rich compounds were observed in the SEI layer containing $Li_2O$, $Li_2O_2$, and $Li_2CO_3$. It should be noted that 75% of $Ge^{4+}$ ions were reduced to $Ge^{3+}$ and metallic Ge from the deconvolution of Ge 3d spectra at the 150 nm depth. The interphase formation was observed by a continuously decreased semicircle in the Nyquist plot from EIS measurement over the initial 18 h, which remained constant for the next two days and then gradually increased over 50 days (Figure 4e). The continuous increase in resistance was accompanied by the formation of small cracks and finally the pulverization of LAGP. Accordingly, the LAGP failure mechanism was explained by the potential chemical gradient of Li and electrons in Li metal, the interphase, and LAGP (Figure 4f). When LAGP is in contact with Li metal, the interphase is chemically formed with mixed ionic and electronic conduction. As an external current is applied to Li/LAGP/Li cell, most of the Li ions and electrons meet at the Li/LAGP interface, acting as a new negative electrode. The reduction of Li at the interphase enables the formation of extra Li oxide-related compounds, which causes a local volume expansion. Long-term cycling can lead to cracks or fractures in LAGP to block Li-ions conduction, thus mechanically damaging the LAGP SE. The lithium oxide compounds at the LAGP/Li interface were formed with the existence of C at the LAGP/Li interface and O from LAGP as the following suggested reaction mechanism. $Li_{1.5}Al_{0.5}Ge_{1.5}(PO_4)_3 + aLi + bC \rightarrow Li_{1.5+x}Al_{0.5}Ge^{4+/3+}{}_{1.5}(PO_{4-\delta})_3 + cLi_2O + dLi_2O_2 + bLi_2CO_3$

The loss of O from LAGP changes the stoichiometry of LAGP and causes the reduction reaction of $Ge^{4+}$ to maintain the charge neutrality (Figure 4g). Sottos' group[66] constructed a Li/LAGP/Au solid cell and tracked the in situ strain distribution. A spatially heterogeneous strain distribution was investigated during the lithiation/delithiation sweep. The localized highly deformed domains are likely to induce mechanical degradation (crack or fracture) in LAGP SE.

### 3.2. Interface Modification Strategies for the Li/LAGP Interface

Based on these observations and findings, the stabilization of the Li/LAGP interface is a top priority for the further develop-

**Table 2.** Performance summary of Li||LAGP||Li symmetrical cells with interlayers.

| Battery configuration | Interlayer thickness [μm] | Ionic conductivity [25 °C, S $cm^{-1}$] | Electrochemical stability window of LAGP/interlayer [V] | Pretreatment | Interfacial stability against Li | Current density [mA $cm^{-2}$ × h] | Working temperature [°C] | Ref. |
|---|---|---|---|---|---|---|---|---|
| Li‖LAGP/PCVA‖Li | 5 | $3.34 \times 10^{-4}$ (50 °C) | 4.8 | 50 °C for 30 min | 850 h | 0.05 × 2 | 50 | [72] |
| Li‖aioc-LAGP‖Li | 11 | $1.21 \times 10^{-4}$ (50 °C) | 4.3 | 50 °C for 4h | 200 h | 0.05 × 4 | 30 | [73] |
| Li‖l-SN/LAGP/l-SN(10 μL solution)‖Li | — | $2.09 \times 10^{-4}$ | — | — | 400 h | 0.1 × 2 | 40 | [74] |
| Li‖AAPP/CB@PP@ LAGP(25 μL electrolyte)‖Li | 10 | $1.13 \times 10^{-3}$ | — | — | 400 h | 1 × 1 | R.T. | [75] |
| Li‖LAGP/LAGP-IL‖Li | — | — | — | — | 1500 h | 0.1 × 1 | R.T. | [71] |
| Li‖SPI-LAGP-SPI‖Li | 10 | $1.4 \times 10^{-4}$ | 4.8 | 60°C for 6h | 600 h | 0.1× 1 | R.T. | [69] |
| Li‖PVCA/$SiO_2$-LAGP-PVCA/$SiO_2$‖Li | — | — | — | — | 1600 h | 0.1× 1 | R.T. | [76] |
| Li‖CSSE‖Li | 50 | $2.71 \times 10^{-4}$ | 4.6 | — | 1000 h | 0.1 × 10 | R.T. | [77] |
| Li‖Cr on $Al_2O_3$/LAGP/Cr on $Al_2O_3$‖Li | 30 nm Cr on 6 nm $Al_2O_3$ | — | — | — | 1200 h | 0.2 × 1 | R.T. | [78] |
| Li‖Ge/LAGP/Ge‖Li | 30 nm | $2.1 \times 10^{-4}$ | — | — | 200 | 0.1 × 1 | R.T. | [67] |
| Li‖3DGPE/LAGP/3DGPE‖Li | — | — | — | — | 250 | 0.1 × 1 | R.T. | [79] |

ment of LAGP-based ASSLB.[4b] **Table 2** summarizes recent interlayer strategies for Li-LAGP interfacial stabilization. Zhou et al.[67] sputtered an amorphous Ge layer on the LAGP surface to suppress the reduction of $Ge^{4+}$ ions and ensure intimate contact between LAGP SE and Li metal (**Figure 5**a). The coating layer was ≈60 nm, as seen in the cross-sectional SEM image (Figure 5b). Notably, the interfacial resistance of Li/LAGP/Li symmetrical cell dropped from 2506 to 147 Ω after Ge film coating due to the good wettability of Ge toward metallic Li. The pristine Li/LAGP/Li had a rapid increase in overpotential after 25 Li plating/striping cycles at 0.1 mA $cm^{-2}$, whereas the Ge-coated cell exhibited an extended cycling lifetime (100 cycles) with small and stable charge/discharge overpotential. Liu et al.[68] deposited 500-nm Li phosphorous oxynitride (LiPON) film by radio-frequency magnetron sputtering on the surface of LAGP-PEO composite electrolyte to ensure a uniform $Li^+$ flux and suppress the formation of Li dendrites.

In addition, Zhou's group[69] developed an in situ solidifying strategy to introduce a succinonitrile-based solid polymer interlayer (SPI) at the Li/LAGP interface (Figure 5c). This polymer well-filled voids or cracks at the solid-solid surface and effectively facilitated Li-ion conduction (Figure 5d). In particular, no Ge reduction was observed from Ge 3d XPS spectra for SPI-protected cycled LAGP (Figure 5e). Consequently, the SPI-based symmetric cell had a 600-h cycling time at 0.1 mA $cm^{-2}$ and a high critical current density of 7 mA $cm^{-2}$. Yu et al.[70] designed a self-sacrificed interface to achieve intimate contact between Li metal and LAGP/poly(propylene carbonate) (PPC) solid electrolyte. The interfacial reaction between Li metal and PPC induced the formation of a LiF-rich SEI layer to suppress Li dendrites deposition.

Moreover, Xiong et al.[71] designed a quasi-solid-state paste as a functional layer to create a chemically stable interphase. As illustrated in Figure 5f, LAGP nanoparticles, (*N*-Methyl-(*n*-butyl) imidazolium bis(fluorosulfonyl)imide, BMIM-FSI ionic liquid (IL) and Li salt (LiFSI) were ball-milled to form a gel-like paste. This unique layer enabled a 1500-h cycling time with a low overpotential of 30 mV in a Li symmetrical cell (Figure 5g). However, the liquid electrolyte-wetted Li/LAGP/Li cell showed a much larger overpotential and shortened cycle life and finally ended up with a sudden short circuit. This excellent cycling stability was attributed to the generation of LiF induced by the breakdown of BMIM-FSI throughout the SEI layer. On the other hand, this LAGP-IL layer addressed the thermal runaway issue of LAGP when contacting molten Li. The bare LAGP was reported to show three stages of floating, cracking, and a super-bright flash (Figure 5h) within 4 min. In contrast, the LAGP-IL coated LAGP had good wettability toward molten Li, and no thermal reaction occurred after 40 min. The enhanced thermal stability benefited from the protection of amorphous carbon that was generated by the decomposition of ionic liquid cation and anion. As a result, crystalline LAGP was separated by the carbon layer, and the thermal runaway was prevented during the heating process.

### 3.3. LAGP/Cathode Interface

#### *3.3.1. The effect of Space-Charge Layers on the Li-Ion Transport at the LAGP/Cathode Interface*

The LAGP/cathode interface also suffers from poor Li-ion transport that originates from the electrochemical decomposition of LAGP or the volumetric change accompanied by the decomposition.[17] Moreover, the charge transport is affected by the space-charge layers (electrochemical double layers) formed at the electrode-electrolyte interface due to the local charge carrier depletion or enrichment.[80] The 2D exchange nuclear magnetic resonance spectroscopy (NMR) is a critical method for identifying structural evolution and Li-ion

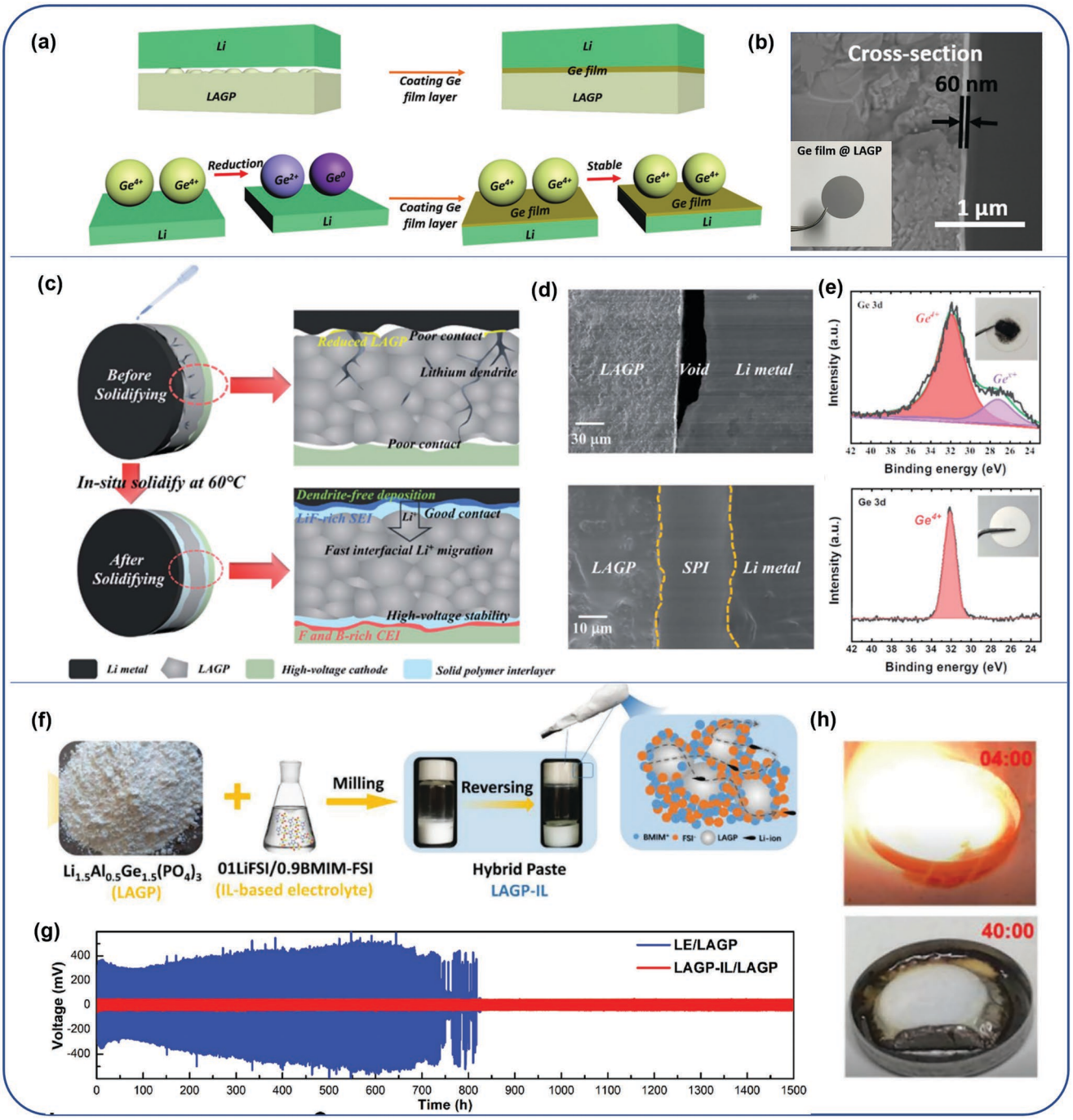


**Figure 5.** Stabilization of Li/LAGP interfaces by multiple interlayers. a) Amorphous Ge film coating on LAGP and b) SEM image of Ge-coated LAGP. Reproduced with permission.[67] Copyright 2018, Wiley-VCH GmbH. c) In situ solidification of succinonitrile-based solid polymer interlayer on LAGP, d) SEM images of Li/LAGP interface with/without SPI modification, e) Ge 3d XPS spectra of cycled LAGPs with/without SPI modification. Reproduced with permission.[69] Copyright 2020, The Royal Society of Chemistry. f) Schematic diagram of LAGP-IL hybrid paste preparation, g) voltage profiles of Li|LAGP pellet|Li symmetric cells with a LAGP-IL interlayer or liquid electrolyte at a current density of 0.1 mA $cm^{-2}$ and a capacity density of 0.1 mAh $cm^{-2}$, h) images of LAGP pellet in contact with Li at 300 °C. Reproduced with permission.[71] Copyright 2020, Wiley-VCH GmbH.

diffusion pathways at solid electrolytes and solid-solid interfaces. By changing the $Li_xV_2O_5$ potential, the space-charge layer between LAGP and $Li_xV_2O_5$ cathode was tuned systematically.[81] The 2D exchange NMR indicated a significant increase in the activation energy for Li-ion conduction over the LAGP-$Li_xV_2O_5$ interface. The higher activation energy eventually contributed to the larger battery internal resistance. The following sections summarize several feasible strategies to mitigate the space-charge layer effect at the LAGP/cathode interfaces.

**Table 3.** Cell performance of LAGP-based solid-state Li-ion batteries.

| Battery configuration | Cathode loading [mg cm$^{-2}$] | Pre-treatment | Operating voltage [V] | Initial discharge capacity [mAh g$^{-1}$] | Cycling capacity retention | Working temperature [°C] | Ref. |
|---|---|---|---|---|---|---|---|
| Li‖PVCA‖LAGP‖2 µL precursor solution ‖LFP | 1.2 | 50 °C for 30 min | 2.8–4 | 153 | 96% after 200 cycles at 0.5C | 50 | [72] |
| Li‖aioc-LAGP‖LFP | 1.5 | 50 °C for 4 h | 2.5–3.8 | 120.1 | 86.4% after 100 cycles at 0.5C | 50 | [73] |
| Li‖l-SN/LAGP/l-SN(10 µL solution)‖LFP | — | — | 2.8–4.0 | 168.4 | 93.17% after 100 cycles at 0.5C | 40 | [74] |
| Li‖LAGP/LAGP-IL‖LFP | 5 | — | | 150 | 0.053% fading for 200 cycles at 0.3C | R.T. | [71] |
| Li‖SPI-LAGP-SPI‖NCA | 2–3 | 60 °C for 6 h | 2.75–4.3 | 200 | 80% after 100 cycles at 0.5C | R.T. | [69] |
| 3D ASSLiB with NCM811 | 13 | | 3–4.25 | 2.01 mAh cm$^{-2}$ | 70% after 50 cycles at 0.1C | 60 | [84] |
| Li‖CSSE‖LFP | 3.92 | — | 2.5–4.0 | 153.4 | 95.3% after 100 cycles at 0.1C | R.T. | [77] |
| PAALi/$RuO_2$/CNT‖LAGP‖LNMO/CNT/PAALi | — | — | 0.8–4.1 | 87.5 | 120 cycles at 0.2C | R.T. | [94] |
| Li‖LAGP-LATP‖LFP | — | — | 2.5–4.0 | 130.6 | 5 cycles at 0.1C | R.T. | [95] |
| Li‖LAGP@glass‖LFP | 1.5 | — | 2.8–3.8 | 152.2 | 93.6 after 120 cycles at 0.1C | 60 | [96] |

### *3.3.2. LAGP/Li-Ion Cathode*

The comparison of full cell performance of LAGP-based solid-state Li-ion batteries is listed in **Table 3**. As discussed in Section 2.4, thinner SEs have lower internal resistance, thus enabling efficient Li-ion conduction and higher energy density. In this case, the high-loading cathode can be assembled with thin LAGP film for better utilization of active materials (**Figure 6**a), as studied by Amine's group.[16b] They fabricated a 60-µm LAGP thin film and a 30-µm LAGP/LFP cathode with a high loading of 8 mg cm$^{-2}$ (Figure 6b), and the Li/ionic-liquid interlayer/LAGP/LFP cell maintained a reversible capacity of 110 mAh g$^{-1}$ at C/3 after 60 cycles. XANES and EXAFS spectra provide similar energy positions and peak intensities for pristine and cycled LAGP (Figure 6c), revealing the excellent electrochemical and structural stability of LAGP without the formation of new phases or breakdown of crystallinity inside LAGP electrolyte. Additionally, the LAGP/LFP interface stability was analyzed by in situ HEXRD characterization on the LFP/LAGP (50/50, w/w) mixture that was heated at 800 °C (held for 9 h) and naturally cooled. As seen in Figure 6d, the 2-theta positions of the LAGP peak (012) and LFP peaks (200, 210, and 011) shifted to lower angles during the heating process due to thermal expansion and reversibly returned to their original 2-theta positions after cooling down to room temperature. However, an irreversible phase transition was observed for LAGP/NCM811 cathode mixture by in situ heating and XRD characterization. Upon heating, the peak intensities of LAGP and NCM811 cathode were gradually decreased and ultimately disappeared at around 760 °C. Meanwhile, some new peaks appeared corresponding to the $(Ni,Co,Mn)_3(PO_4)_2$ with P21/n space group (Figure 6e).

To repair the SE/electrode interfacial cracks upon cycling, Wang et al.[82] prepared self-healing polymer electrolytes (SHEs) as Janus interfaces for LAGP-based Li metal batteries. They fabricated a stable Li/LAGP/$LiMn_2O_4$ battery (Figure 6f) with integrated electrode/electrolyte contact by anolyte SHE (ASHE) and catholyte SHE (CSHE). ASHE was prepared by in situ polymerization of pentaerythritol tetraacrylate (PETEA) cross-linker and 2-[3-(6-methyl-4-oxo-1,4-dihydropyrimidin-2-yl)-ureido] ethyl methacrylate (UpyMA) monomer with 10 wt% ethylene carbonate (EC) added 0.5 M bis(trifluoromethane)sulfonimide lithium salt (LiTFSI) in 1-ethyl-3-methylimidazolium bis-(trifluoromethylsulfonyl)imide (EMITFSI). SHE (CSHE) was obtained by in situ polymerizing UpyMA-PETEA copolymer with adiponitrile (AN)-added electrolyte due to the high resistance of AN against electrochemical oxidation. DFT simulation revealed that UpyMA–UpyMA clusters had more negative formation energy (–2.03 eV) than clusters between the UpyMA monomer and PETEA (–0.53 eV), $EMITFSI^-$ (–0.97 eV), and AN (–0.88 eV). Consequently, the UpyMA units in the polymer chains tended to form abundant intermolecular or intramolecular hydrogen bonds,[83] thus leading to the excellent self-healing ability to recover interfacial cracks or mechanical damage. After cycling, uneven Li deposition was observed on the surface of Li metal, and the SEI layer had a low Young's modulus (475 MPa) (Figure 6g). In comparison, monolithic, smooth, and robust SEI was formed on the Li metal surface with an enhanced Young's modulus of 2549 MPa from the ASHE-based Li metal cell. Compared to the pristine Li/LAGP/$LiMn_2O_4$ battery, the SHE-based cell delivered a higher reversible capacity of 90.0 mAh g$^{-1}$ after 120 cycles (Figure 6h), much smaller interfacial resistance (Figure 6i), and superior rate capability at 0.05–0.5C (Figure 6j).

To improve cathode loading and address the issue of poor SE/electrode interface contact, Huang et al.[84] designed a unique tri-layer solid electrolyte structure consisting of a dense LAGP

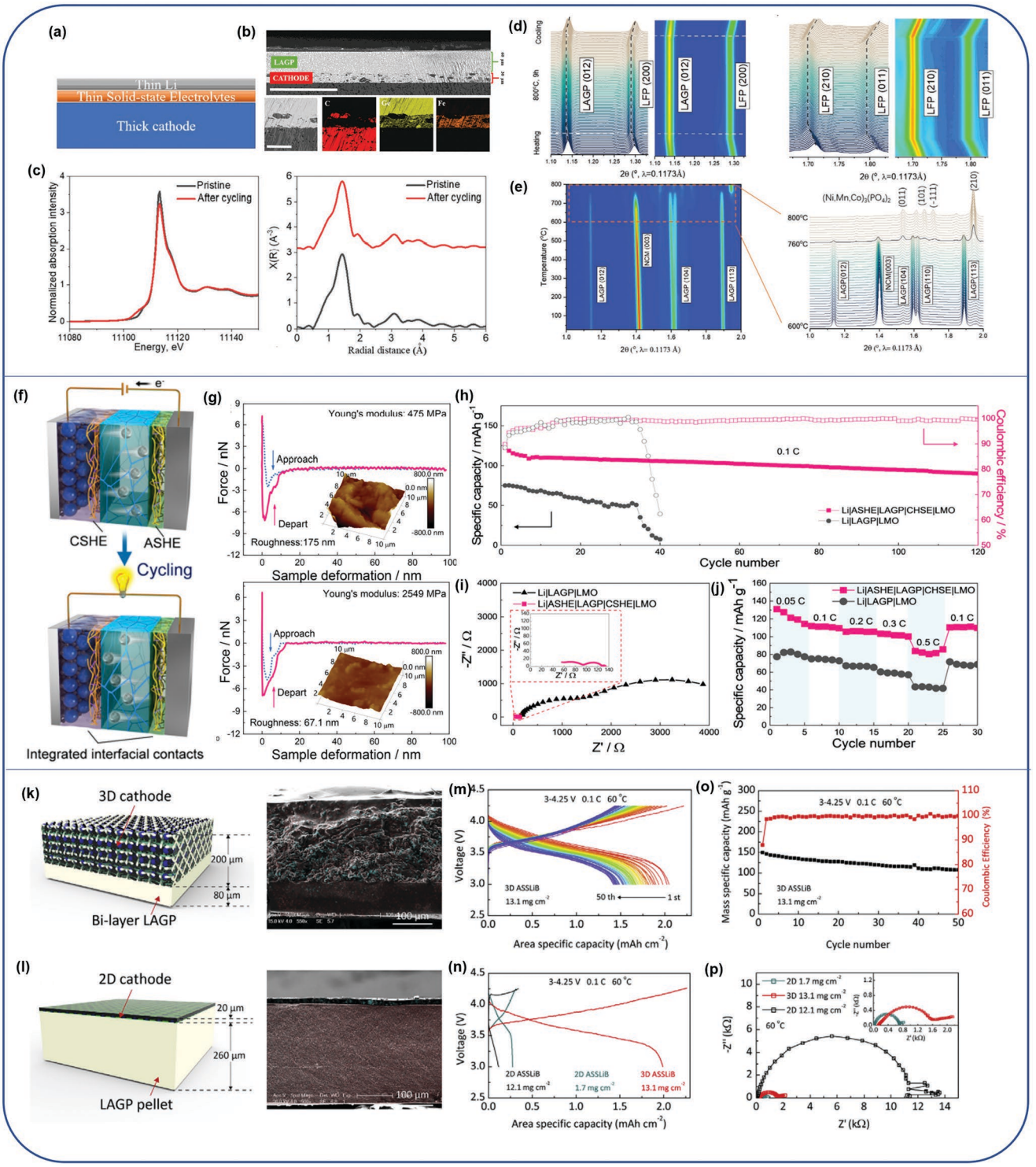


**Figure 6.** a) ASSLB configuration, b) cross-section SEM image of thin LGP-LAGP-graphite cathode/LAGP electrolyte and EDS mapping. Scale bars at the top of (b) and bottom of (b) are 200 and 50 μm, respectively. c) Ge K-edge a) XANES and b) EXAFS spectra of LAGP electrolyte before and after cycling, d) in situ HEXRD patterns and the corresponding contour plot of LAGP/LFP mixture during heating and cooling, I Contour plot and d) in situ HEXRD patterns of LAGP/NCM811 mixture during heating to 800 °C. Reproduced with permission.[16b] Copyright 2021, Wiley-VCH GmbH. f) Li|LAGP|LMO batteries with SHEs as Janus interface layers, g) force–displacement plots of LAGP-derived SEI and ASHE-derived SEI, h) cycling performances of Li|LAGP|LMO and Li|ASHE|LAGP|CSHE|LMO cells at 0.1 C, i) Nyquist plots of the Li|LAGP|LMO cell after 30 cycles and the Li|ASHE|LAGP|CSHE|LMO cell after 120 cycles (inset) at 0.1 C, j) rate performances of the LAGP-based Li metal batteries with and without SHE interface layers. Reproduced with permission.[82] Copyright 2020, American Chemical Society. Schematic and cross-sectional SEM image/EDS mapping of k) 3D and l) 2D cathodes (in the EDS element mappings, blue color corresponded to Ni from NCM811, and red color to Ge from LAGP) m) voltage profiles and n) cycle performance of 3D cathode, o) voltage profile of 2D cathode, and p) Nyquist plots of 2D and 3D cathodes in the first cycle. Reproduced with permission.[84] Copyright 2019, Elsevier.

layer (≈80 µm), porous LAGP support layer (≈250 µm), and polyethylene glycol bis(amine)-triglycidyl isocyanurate (NPEG-TGIC, N-T) solid polymer electrolyte layer (Figure 6k). The dense-porous LAGP bilayer was prepared by a facile templet-casting method to conduct Li-ions and simultaneously act as a cathode host. The NCM811 loading reached up to 13 mg $cm^{-2}$ due to the large surface area (0.54 $m^2$ $g^{-1}$) of the dense-porous LAGP bilayer. In the first charge/discharge cycle, the 3D cathode delivered a high areal specific capacity of 2.01 mAh $cm^{-2}$ and a Coulombic efficiency of 87%. After 50 cycles, the cell retained 109 mAh $g^{-1,}$ corresponding to a 70% capacity retention (Figure 6m,o). As a comparison, cathode slurry was cast on a 260 µm-thick LAGP pellet to form a 20-µm 2D cathode (Figure 6l), which had much lower NCM loading (1.76 mg $cm^{-2}$) and areal capacity (0.27 mAh $cm^{-2}$) in the initial cycle (Figure 6n). With NCM loading increasing to 12.16 mg $cm^{-2}$ for the 2D cathode, the impedance dramatically increased to 11000 Ω (vs. 1600 Ω for the 3D cathode), implying the inferior interface contact between the 2D cathode layer and LAGP pellet (Figure 6p). Moreover, GITT data suggest that the 3D cathode possessed a smaller polarization and higher Li-ion diffusion coefficient ($2.9 \times 10^{-11}$ $cm^2$ $s^{-1}$) than the 2D cathode ($0.7 \times 10^{-11}$ $cm^2$ $s^{-1}$).

### 3.3.3. Li–$O_2$ Battery

In addition to solid-state lithium-ion batteries, LAGP SE is also applied in lithium-sulfur or lithium-oxygen batteries.[46,75,85] Sun et al.[86] prepared LAGP-NCNT-$Li_3InCl_6$ air electrode (NCNT stands for nitrogen-doped carbon nanotubes) with halide electrolyte $Li_3InCl_6$ as a superionic conductor. As shown in **Figure 7**a, $Li_3InCl_6$ was uniformly distributed within the air electrode to enable intimate contact with NCNT and LAGP. The point contact between LAGP ionic conductor and NCNT electronic conductor in the LAGP-NCNT air electrode was unfavorable for ion or electron transport. With the modification of superionic conductive $Li_3InCl_6$, redox kinetics were boosted, and more discharge products were decomposed to ensure the good stability of a Li–$O_2$ battery. Figure 7b presents the distributions of C, Cl, and O elements in the discharged LAGP-NCNT-0.5$Li_3InCl_6$ through STXM averaging stack images at each elemental edge. The similar shape and contrast indicate the uniform distribution of these elements. The peak located at 531.5 eV in O K-edge XANES spectra (Figure 7c) was attributed to $\sigma^*$ (O—O) peak characteristic of $Li_2O_2$. At the current density of 100 mA $g^{-1}$, the LAGP-NCNT-0.5$Li_3InCl_6$ electrode delivered

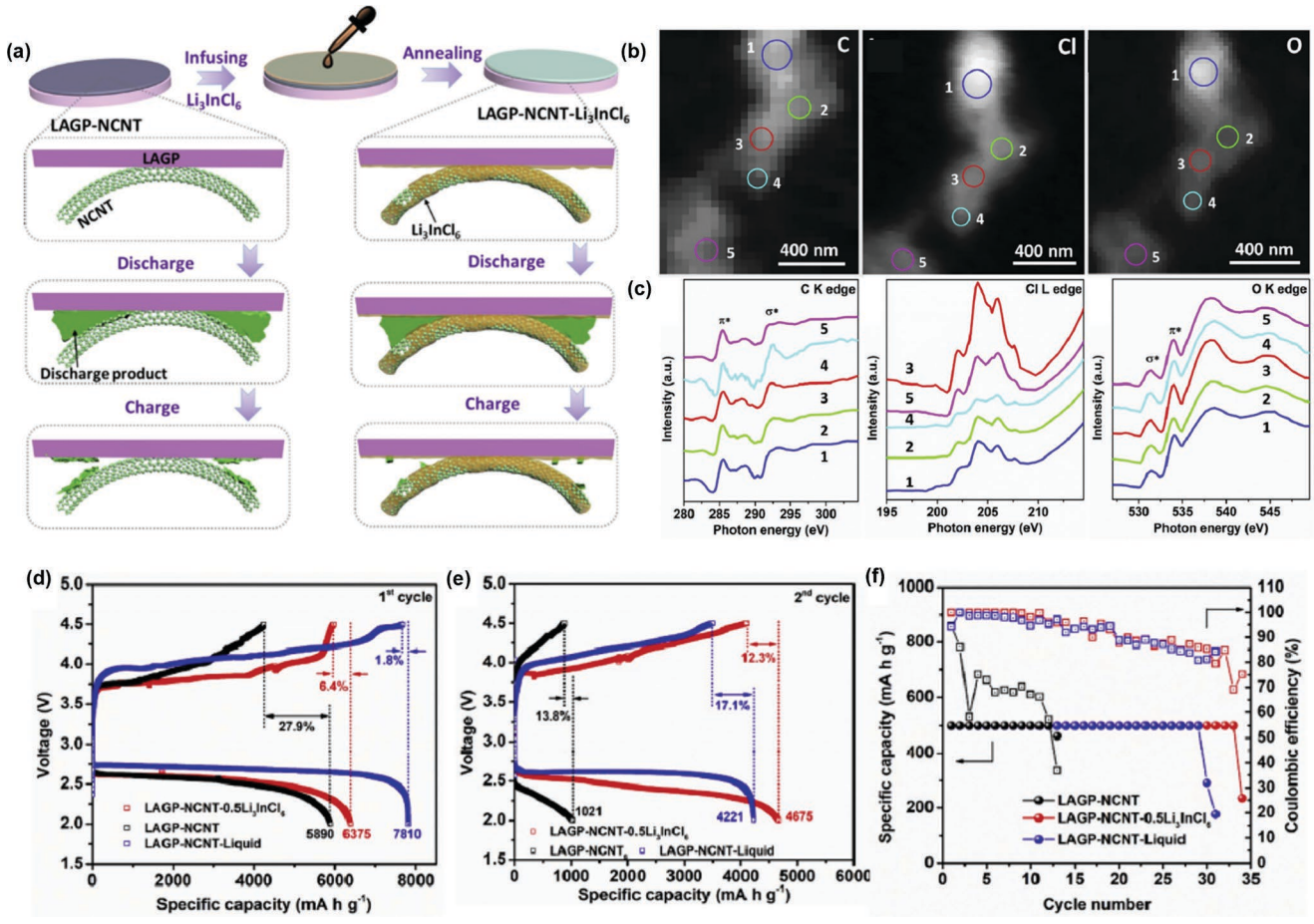


**Figure 7.** a) Schematic illustration of LAGP-NCNT-$Li_3InCl_6$ air electrode preparation and the effect of a $Li_3InCl_6$ modifier on the decomposition of discharge products, b) STXM optical density images of C, Cl, and O distributions in the discharged LAGP-NCNT-0.5$Li_3InCl_6$ and c) corresponding XANES spectra of the C K-edge, Cl L-edge, and O K-edge, d) 1st cycle and 2nd cycle discharge/charge profiles of the Li–$O_2$ battery at 100 mA $g^{-1}$ with LAGP-NCNT, LAGP-NCNT-0.5$Li_3InCl_6$, and LAGP-NCNT-liquid air electrodes, respectively. f) Cycling performance of LAGP-NCNT-0.5$Li_3InCl_6$, and LAGP-NCNT-Liquid air electrodes. Reproduced with permission.[86] Copyright 2020, Elsevier Ltd.

significantly increased capacities of 6375 and 4675 mAh $g^{-1}$ in the first and second cycle, respectively, as well as higher initial Coulombic efficiency of 93.6% (vs. 5890/1021 mAh $g^{-1}$, 72.1% CE for LAGP-NCNT electrode), as shown in Figure 7d–f.

#### 3.3.4. LAGP/S Interface

The LAGP-based Li–S batteries also suffered from poor LAGP/electrode interfacial contact, Li/LAGP interface instability, and the "shuttle effect" caused by the dissolution of polysulfides.[87] To overcome these interface issues, Wen et al.[85c] introduced a flexible ionic conductive composite polymer electrolyte to stabilize Li/LAGP interface and drew an electronic conductive graphite layer on LAGP facing S cathode with a pencil, as shown in **Figure 8**a,b. This modified LAGP electrolyte significantly improved cycling stability with 1080 mAh $g^{-1}$ retained after 150 cycles at 0.1 C (Figure 8c). The two discharge plateaus at 2.3 and 2.05 V in Figure 8d corresponded to the reduction from $S_8$ to polysulfides and sulfides, respectively. The graphite layer was found to effectively confine the reduction production of $S_8$ within the conductive network as a second current collector. The reliability of the modified LAGP electrolyte was furtherly found in a soft-package Li-S battery with a well-maintained capacity for 40 cycles (Figure 8e). This all-solid-state Li–S cell lighted up light-emitting diode (LED) lamps which were even brighter while being burned due to the higher ionic conductivity of solid electrolytes at elevated temperatures (Figure 8f).

Moreover, the semi-solid-state Li–S batteries gained much attention due to the facilitated Li-ion/electron transfer at the electrode/electrolyte interface by hybrid electrolytes.[75,88] Wen's group[89] introduced a hybrid electrolyte composed of LAGP and FDE (FDE, 1,3-(1,1,2,2-tetra-fluoroethoxy)propane)) to decrease interfacial resistance, avoid the loss and redistribution of active sulfur on cathodes, as well as suppress the dissolution of polysulfides by the highly fluorinated FDE (**Figure 9**a). Manthiram et al.[90] presented a hybrid Li–S based on a gel sulfur cathode, LAGP solid electrolyte, a thin layer of glass fiber filled with high-concentrated anolyte (3 M $LiCF_3SO_3$ containing $Li_2S_6$ and $LiNO_3$), as well as Li anode, as shown in Figure 9b. The gel sulfur cathode was prepared by dropping $Li_2S_6$ solution onto the PVDF-HFP/carbon paper and was expected to entrap polysulfides while allowing fast ionic transport. The hybrid cell delivered high capacities of 1086, 986, 772, and 650 mAh $g^{-1}$ at current densities of 0.1, 0.2, 0.3, and 0.4 mA $cm^{-2}$ (Figure 9c). The Li/LAGP interface was furtherly visualized by TOF-SIMS depth profiling and mapping on the cycled LAGP (Figure 9d–f). It was revealed that a solid-liquid electrolyte interphase (SLEI) layer containing $F^-$, $SO^-$, and $C^-$ was formed between LAGP solid electrolyte and liquid electrolyte during extensive cycling. This advanced cell configuration effectively suppressed the shuttle effect and Li dendrite growth and reduced the consumption of liquid electrolytes.

#### 3.3.5. LAGP/$I_2$ Interface

The low-cost, environmentally friendly, and high-capacity (211 mAh $g^{-1}$) Li–$I_2$ battery is another promising battery system for large-scale energy storage.[91] The sluggish one-step redox conversion ($I_2 + 2e^- \rightarrow 2I^-$) and poor solid–solid interfacial contact are two main challenges in conventional solid-state Li–$I_2$ batteries.[92] Recently, LAGP has been used in Zhou's research group[93] as a blocking layer to mitigate the shuttle effect of polyiodides in a solid-state Li–$I_2$ battery. The Li-ion exchange observed in 2D NMR revealed a fast Li-ion conduction at the PEO/LAGP interface. It is also found that the LAGP blocking layer could localize the dissolution of polyiodides near the $I_2$ cathode, while the PEO dispersion layer facilitated the two-step redox reaction by $I_5^-/I_3^-$ and $I_3^-/I^-$ redox couples and Li-ion transport in all-solid-state Li-$I_2$ batteries. This well-designed hybrid electrolyte enabled a long cycle life of over 9000 cycles with 84.1% capacity retention at 1C.

## 4. LAGP/Polymer/Salt Composite Solid Electrolytes

Polymer/ceramic composite solid electrolytes (CSEs) are gaining intense attention as CESs show not only good flexibility and intimate interfacial contact but also high ionic conductivity, mechanical strength, and electrochemical stability.[13b,97] Generally, LAGP-based CSEs are composed of polymer (e.g., PEO, PVDF, PVDF-HFP), LAGP, and Li salt (e.g., LiTFSI). Polyethylene oxide (PEO) is widely investigated as a polymer matrix mainly due to its good ability to solvate a wide variety of Li salts through the interaction between the ether oxygens in PEO and cations in Li salt.[97c] The addition of inorganic particles such as LAGP can form a $Li^+$ pathway and simultaneously enhance the mechanical properties.[98] The preparation for CSE can be divided into blending/solution casting, cold/hot-pressing, ice-plating, and 3D printing. **Table 4** summarizes the thickness, ionic conductivities, and electrochemical stability of polymer/LAGP composite electrolytes, and the cycling performance of solid-state full cells.

Blending, incorporating LAGP particles into a polymer matrix followed by a solution casting step, is the most common method for fabricating hybrid LAGP/polymer electrolytes.[68,99] Xu et al.[99a] incorporated glass-ceramic LAGP particles with a wide grain size of 1–30 µm into PEO matrix to prepare homogeneous CSEs with a 200 µm thickness. The ionic conductivity increased from $4.29 \times 10^{-4}$ (PEO only) to $6.76 \times 10^{-4}$ S $cm^{-1}$ (LAGP-PEO with the smallest grain size below 1 µm) at 60 °C. The enhanced ionic conductivity was due to the reduced crystallization and weakened interactions between $Li^+$ and PEO chains by the introduction of LAGP. With LAGP particle size increasing, the ionic conductivity of PEO-LAGP electrolyte gradually decreased because smaller LAGP particles had a larger contact area with PEO polymer and more effectively suppressed PEO crystallization.[100] The incorporation of LAGP fillers also improved tensile strength owing to the plasticizer effect and extended electrochemical stability window to 5.1 V resulting from the suppression of PEO decomposition. The mechanical properties (ductility, elongation at break, tensile strength) are also affected by the inhomogeneity of particle distribution and particle size.[98] Song et al.[101] designed PPLS (PVDF-HFP/PEO/LAGP/SIL) (SIL stands for solvate ionic liquid) solid electrolytes using organic PVDF-HFP to provide mechanical support. As

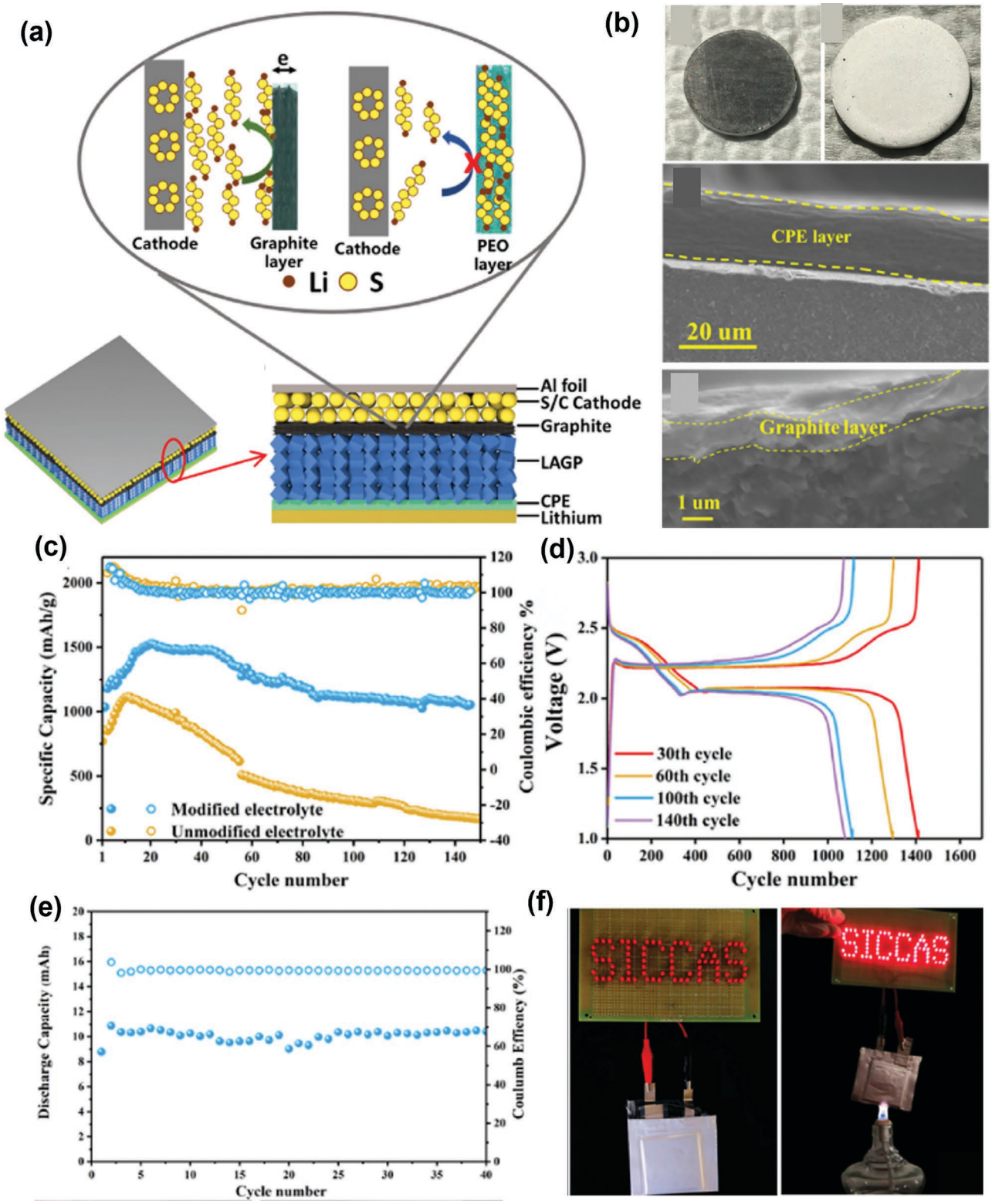


**Figure 8.** a) All-solid-state Li/LAGP/S batteries with graphite and CPE layers, b) optical photos of LAGP drawn by graphite and coated by CPE, cross-sectional SEM images of LAGP-CPE and LAGP-graphite, c) cycling performance of Li/LAGP/S cells with/without graphite and CPE layers at 0.1C, d) charge–discharge curves of Li–S batteries with modified LAGP, e) cycling performance of the soft package Li–S cells with modified LAGP, f) Li–S cell lights up the "SICCAS" LED lamps at the connected circuit and burning status, respectively. All Li–S batteries are tested at 60 °C. Reproduced with permission.[85c] Copyright 2019, Elsevier.

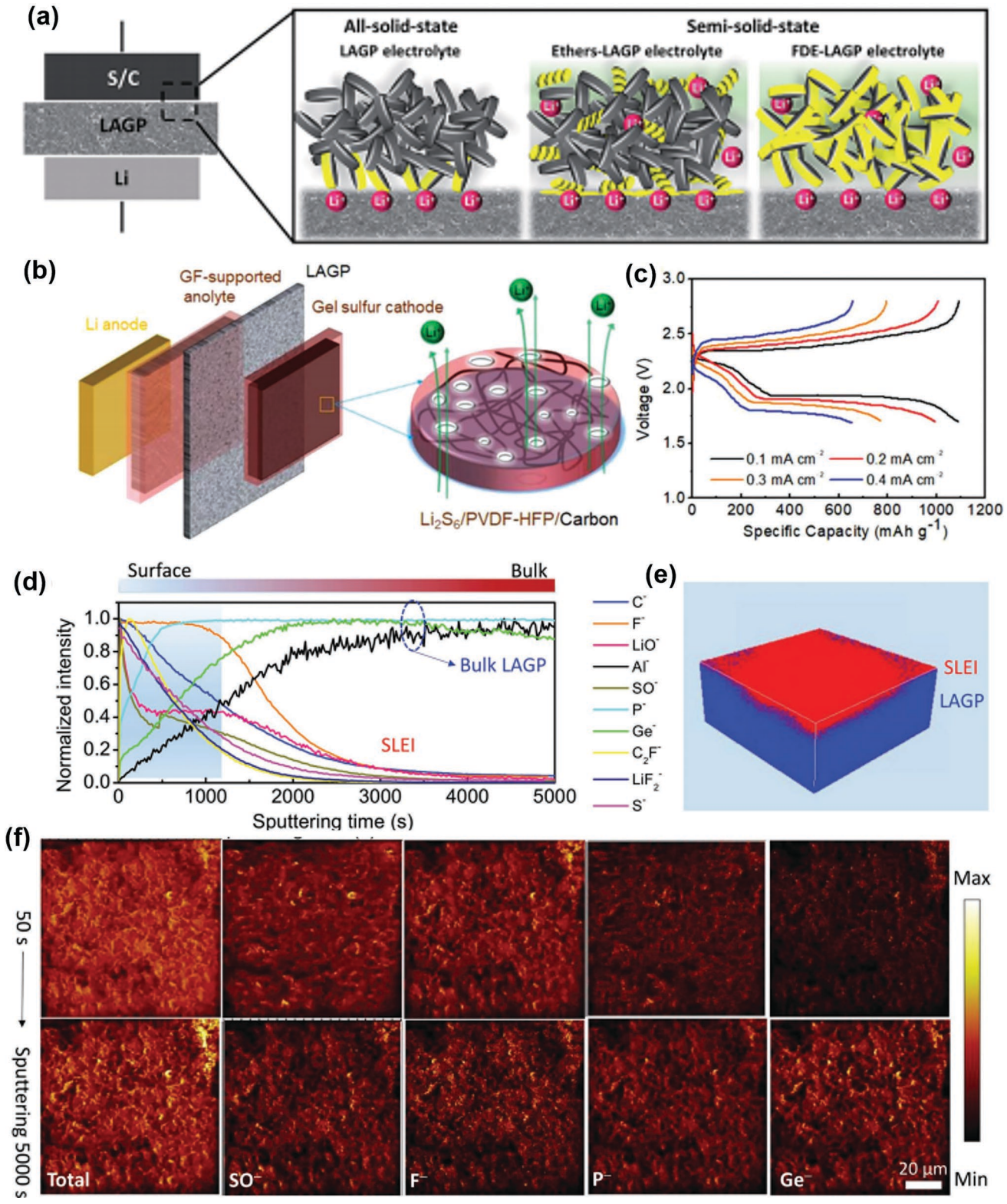


**Figure 9.** a) Schematic of semi-solid-state Li–S batteries. Reproduced with permission.[89] Copyright 2017, The Royal Society of Chemistry. b) Schematic illustration of the hybrid cell structure, where the PVDF-HFP/carbon/$Li_2S_6$ served as a gel cathode, LAGP as a solid electrolyte, Li metal as an anode, and 3 M $LiCF_3SO_3$ containing $Li_2S_6$-$LiNO_3$ as an anolyte, c) charge–discharge curves at 0.1–0.4 mA $cm^{-2}$, d) normalized TOF-SIMS depth profiles of a series of secondary ion fragments of interest collected at the surface of the cycled LAGP pellet in a negative mode, e) a 3D view of the element distribution in the TOF-SIMS sputtered volumes of cycled LAGP, f) TOF-SIMS chemical mapping collected after 50 and 5000 s $Cs^+$ etching. Reproduced with permission.[90] Copyright 2018, Wiley-VCH GmbH.

**Table 4.** Performance summary of polymer/LAGP-based solid-state batteries.

| Solid electrolyte | Preparation method | Thickness [μm] | Ionic conductivity [25 °C, S $cm^{-1}$] | Electrochemical stability window [V] | Interfacial stability against Li | Full cell configuration | Capacity retention | Ref. |
|---|---|---|---|---|---|---|---|---|
| PVDF-HFP/LAGP | Electrospinning and dip-coating | 85 | $3.18 \times 10^{-3}$ | 5.3 | 1000 h at 2 mA $cm^{-2}$ | Li‖PVDF-HFP/LAGP‖NCM811 | 84.5% after 500 cycles at 0.2C | [117] |
| LAGP/SN | In situ thermal polymerization | — | $1.17 \times 10^{-3}$ (30 °C) | 5.0 | 200 h at 0.2 mA $cm^{-2}$ | Li‖PVDF-HFP/LAGP‖NCM523 | 90.0% after 100 cycles at 0.2C | [112] |
| LAGP@PVDF-HFP shell | Solution casting | — | — | — | 350 h at 0.2 mA | Li‖LAGP@PVDF-HFP‖Ru-CNT (Li-$O_2$) | 146 cycles at 300 mA $g^{-1}$ | [118] |
| PVDF-HFP/LAGP/EMITFSI | Solution casting | 150 | $4.49 \times 10^{-3}$ | — | — | Li‖ PVDF-HFP/LAGP/EMITFSI ‖LFP | 151 mAh $g^{-1}$ after 50 cycles at 0.05C | [106] |
| LAGP@PEO | Cold-pressing | — | $4.4 \times 10^{-5}$ | 5.1 | 1500 h at 0.05 mA $cm^{-2}$ (50 °C) | Li‖ LAGP@PEO ‖LFP | 92.0% after 100 cycles at 0.1C (50 °C) | [107] |
| LAGP/PEO/PEGDA/LiTFSI | Solution casting | 70 | $3.6 \times 10^{-6}$ | — | — | — | — | [111] |
| ASHE/LAGP/CHSE | In situ polymerization | 320 | $2.75 \times 10^{-3}$ | — | 700 h at 0.1 mA $cm^{-2}$ | Li‖ ASHE/LAGP/CHSE ‖$LiMn_2O_4$ | 80.3% after 120 cycles at 0.1C | [82] |
| $PH_{0.35}PGI_{0.15}LEL$ | Solution casting | 200 | $5.79 \times 10^{-4}$ | — | 750 h at 0.02–0.1 mA $cm^{-2}$ | Li‖ $PH_{0.35}PGI_{0.15}LEL$ ‖LFP | 135.2 mAh $g^{-1}$ after 100 cycles at 0.05C | [103] |
| PEO/LAGP/LiTFSI | Solution casting | 58–75 | $3.8 \times 10^{-6}$ | — | — | — | — | [98] |
| LAGP-LiTFSI | Cold sintering | 400 | $2.3 \times 10^{-4}$ | — | 1800 h at 0.1 mA $cm^{-2}$ | — | — | [52] |
| PEO/LAGP | Solution casting | 200 | $1.6 \times 10^{-5}$ | 4.5 | 100 h at 0.2 mA $cm^{-2}$ at 60 °C | Li‖ PEO/LAGP ‖LFP | 60 cycles at 0.1–2C at 80 °C | [108] |
| LAGP/PPC | Solution casting and pressing | — | $1.55 \times 10^{-4}$ (55 °C) | 4.6 | 100 h at 0.01–0.05 mA $cm^{-2}$ | Li‖ LAGP/PPC ‖LFP | 92.3% after 100 cycles at 0.05C at 55 °C | [70] |
| LAGP-PEO | Solution casting | 100–200 | $1.67 \times 10^{-4}$ | 4.5 | 400 h at 0.1–0.3 mA $cm^{-2}$ at 60 °C | Li‖LAGP-PEO‖LFP | 87.4% after 400 cycles at 0.6C at 60 °C | [110] |
| LAGP-PEO | Solution casting and precycling | 76 | $9 \times 10^{-5}$ (50 °C) | — | 400 h at 0.05 mA $cm^{-2}$ at 50 °C | Li‖LAGP-PEO‖PEO-LiTFSI‖LFP | 96% after 200 cycles at 0.1C at 60 °C | [99c] |
| PBA-LAGP | Solution casting | — | — | 4.7 | — | Li‖PBA-LAGP ‖NCM622 | 100 cycles at 0.2C at 55 °C | [104] |
| LAGP-PVDF | Solution casting | 25 | $10^{-4}$ | — | 300 h at 1 mA $cm^{-2}$ | Li‖ LAGP-PVDF(liquid electrolyte)‖Celgard 2400 ‖S/C | 72.1% after 100 cycles at 0.5C | [119] |
| LAGP-PEO(LiTFSI) | Solution casting | 60 | — | — | — | Li(LiPON)‖ LAGP-PEO(LiTFSI)‖LFP | 150 cycles at 0.2C at 50 °C | [68] |
| PVDF-HFP/LAGP/ionic liquid | Solution casting | — | $9.6 \times 10^{-4}$ | 4.8 | 400 h at 0.2 mA $cm^{-2}$ | Li‖ PVDF-HFP/LAGP/ionic liquid ‖LFP | 89.5% after 50 cycles at 0.05C | [99b] |
| LAGP-PEO(LiTFSI) | Solution casting | — | — | 5.12 | — | Li‖PEO-LiTFSI‖ LAGP-PEO(LiTFSI)‖$LiMn_{0.8}Fe_{0.2}PO_4$ | 50 cycles at 0.1C at 50 °C | [79] |
| LAGP/SN/PEO-$LiClO_4$ | Solution casting | 40–50 | $1.1 \times 10^{-4}$ | 5 | 500 min at 0.2 mAh $cm^{-2}$ at 55 °C | Li‖LAGP/SN/PEO-$LiClO_4$‖LFP | 100 cycles at 0.2C | [102] |
| PEO/LAGP | Solution casting | 200 | $6.76 \times 10^{-4}$ (60 °C) | 5.3 (60 °C) | — | Li‖ PEO/LAGP ‖LFP | 90% after 50 cycles at 1C at 60°C | [99a] |
| LAGP/PVDF-HFP | Solution casting | 100 | $2.01 \times 10^{-3}$ | 4.5 | — | Li‖ LAGP/PVDF-HFP (liquid electrolyte) ‖LFP | 96% after 100 cycles at 0.5C | [105] |
| PEO/PVDF-LAGP | Solution casting | 150 | $10.9 \times 10^{-3}$ (30 °C) | 5 | — | Li‖PEO/PVDF-LAGP (liquid electrolyte) ‖LFP | 50 cycles at 0.1C | [120] |

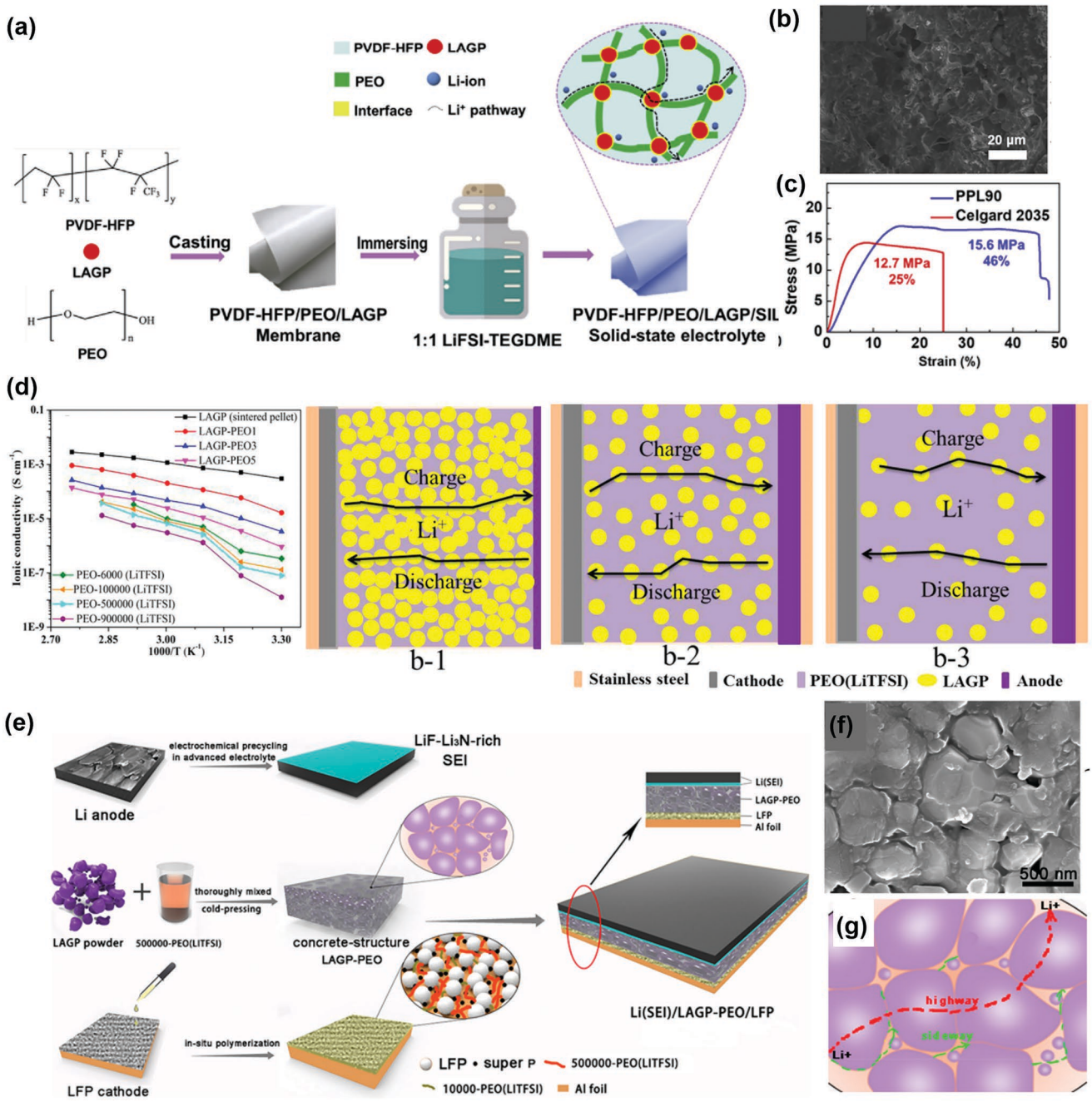


**Figure 10.** a) Schematic of the fabrication process of the PPLS (PVDF-HFP/PEO/LAGP/SIL) solid-state electrolyte by solution casting, b) SEM image, c) stress–strain curve of the PPLS electrolyte. Reproduced with permission.[101] Copyright 2019, Elsevier. d) Arrhenius plots of LAGP pellet and LAGP/PEO composite electrolytes and $Li^+$ transport pathways in LAGP/PEO electrolyte. Reproduced with permission.[79] Copyright 2017, American Chemical Society. e) ASSLB cell configuration with a LAGP/PEO composite electrolyte by cold-pressing, f) SEM image of LAGP/PEO composite electrolyte, and g) $Li^+$ transport pathways. Reproduced with permission.[99c] Copyright 2018, American Chemical Society.

presented in **Figure 10**a, PEO, PVDF-HFP, and LAGP were first dispersed in DMF solvent and formed a uniform membrane by a solution casting method. Subsequently, the dried membrane was immersed in liquid LiFSI:TEGDME for plasticization. Figure 10b,c shows uniform morphology of PPLS electrolyte and high tensile strength (15.6 MPa), respectively. This PPLS electrolyte induced the formation of a LiF-rich SEI layer on Li metal to maintain a dendrite-free morphology, thus enabling an ultralong cycle life (800 h) of Li anode. Ding et al.[79] studied the effect of LAGP content on ionic conductivity and electrochemical performance of LAGP-PEO electrolytes. The relationship of ionic conductivity with temperature for PEO did not follow a classical Arrhenius equation (Figure 10d) due to the coexistence of crystalline and amorphous phases in PEO polymer. The ionic conductivity of LAGP-PEO was higher than that of PEO electrolyte due to faster Li-ion conduction along the LAGP

crystal phase. With LAGP content decreasing, LAGP-PEO composite electrolytes transitioned from "polymer-in-ceramic" to "ceramic-in-salt."

Kim's group[102] added a small amount of high-polarity succinonitrile (SN) in PEO-LAGP-$LiClO_4$ electrolyte to increase the ionic conductivity due to improved Li salt dissolution and decreased crystallinity of PEO by SN. Guo et al.[103] reported a chelating copolymer/LAGP composite electrolyte with LAGP particles coated by a uniform gel polymer layer. This gel polymer layer was synthesized by free radical copolymerization of PVDF (with double bonds) and glyceryl methacrylate (GMA) and then the ring-opening reaction between PVDF-GMA and iminodiacetic acid (IDA). The gel polymer interlayer ensured a soft contact between Li metal and LAGP particles and adapted the volume change during Li plating/stripping, thus leading to a smaller interface impedance and longer lifetime. Kim et al.[104] employed poly(1,4-butylene adipate) (PBA) to fabricate a PBA-LAGP-$LiClO_4$ composite electrolyte due to the higher oxidative stability of ester groups in PBA than ether groups in PEO. Ding et al.[105] prepared a PVDF-HFP-based gel polymer electrolyte showing a wide electrochemical stability window to 5 V. Goswami et al.[106] added ionic liquid 1-ethyl-3-methylimidazolium bis-(trifluoromethylsulfonyl)-imide (EMITFSI) to facilitate $Li^+$ migration in PVDF-HFP/LAGP/LiTFSI composite electrolytes.

However, the agglomeration of ceramic LAGP is hard to completely avoid when preparing composite electrolytes by casting. Using toxic organic solvents (e.g., tetrahydrofuran, dimethylformamide, or acetonitrile) also raises a safety risk. Cold-pressing is a solvent-free approach to obtain composite electrolytes with well-dispersed LAGP in a polymer matrix.[107] Ci et al.[99c] prepared concrete structured LAGP/PEO with a thickness of 76 µm by cold pressing (Figure 10e). The LAGP/PEO had a dense morphology with LAGP particles closely stacked (Figure 10f) to form continuous $Li^+$ migration pathways (Figure 10g), whereas PEO served as a binder to bridge LAGP particles and assist $Li^+$ conduction. To stabilize Li metal anode, ex situ LiF-$Li_3N$-rich SEI layer was generated by precycling the Li anode in an advanced electrolyte of Li bis-trifluoromethanesulfonimide (LiTFSI, 1.0 M)-$LiNO_3$ (1.0 wt%)-1,3-dioxolane (DOL)/1,2-dimethoxyethane (DME)/ fluoroethylene carbonate (FEC) (9:9:2, volume ratio). Ci et al.[107] found that LAGP@PEO by cold-pressing showed nearly one order of magnitude higher ionic conductivity than that by solution casting due to the more uniform distribution of LAGP in the PEO matrix. Gerbaldi et al.[108] hot-pressed solid mixture of PEO, LAGP, and LiTFSI at 80 °C in a dry room to obtain homogeneous, self-standing, and robust composite electrolytes. However, the interface stability between PEO-LAGP-LiTFSI and Li metal remains to be solved.

In addition to randomly dispersed polymer/LAGP composites, vertically aligned nanoparticles have been synthesized by ice-plating and filled by polymer chain and Li salt to form composite electrolytes.[109] Yang et al.[110] fabricated a LAGP/PEO composite electrolyte with vertically aligned LAGP walls providing continuous $Li^+$ transport channels. As illustrated in **Figure 11**a, ice-templated starting suspension was frozen to induce ice crystal growth and generate vertical LAGP walls. After removing ice by vacuum drying, a porous structure was obtained, followed by a sintering treatment at 800 °C. Finally, the PEO polymer was filled into the porous skeleton to obtain the PEO/LAGP composite with vertically aligned LAGP walls. Figure 11b shows well-defined vertically aligned LAGP walls spaced 10–20 µm from each other after ice templating, and the LAGP particles were closer after high-temperature sintering. The introduction of PEO built a bridge to connect LAGP nanoparticles. More importantly, the ice-templated PEO/LAGP had much smaller resistance and higher ionic conductivity ($1.67 \times 10^{-4}$ S cm$^{-1}$) than randomly dispersed PEO/LAGP composite ($1.92 \times 10^{-5}$ S cm$^{-1}$) (Figure 11c). The lower activation energy (0.45 eV) of ice-templated PEO/LAGP (Figure 11d) than that of randomly dispersed composite (0.68 eV) indicated that the LAGP phase played a dominant role in Li-ion conduction. Liu et al.[111] prepared *Z*-direction (out-of-plane) aligned LAGP within cross-linked PEO/PEGDA/LiTFSI driven by a contactless electric field. The aligned nanoparticles were harvested into a polymer chain and separated by a thin polymer layer. This thin interface layer offers an efficient pathway for Li ion transport, thus significantly promoting the ionic conductivity of the composite electrolyte. Wen et al.[112] added ethoxylated trimethylolpropane triacrylate (ETPTA) monomers to fabricate LAGP/SN composites by in situ thermal polymerization. In the LAGP/SN electrolyte, SN polymer was embedded in a vertically aligned LAGP scaffold, and LAGP particles were tightly bonded to form continuous Li-ion transport pathways. Therefore, the LAGP/SN showed a remarkable ionic conductivity ($1.17 \times 10^{-3}$ S cm$^{-1}$ at 30 °C), superior $Li^+$ transference number (0.77), and widened electrochemical window (0–5.0 V vs. $Li^+$/Li). Moreover, a durable solid-state Li-NCM523 battery with LAGP/SN hybrid electrolyte was achieved, delivering a specific capacity of 153.8 mAh g$^{-1}$ after 100 cycles at 0.2 C, corresponding to a capacity retention of 90.0%.

Bruce's group[113] constructed ordered 3D LAGP scaffolds using a 3D printed polymer template and filled the empty channels with epoxy polymer to create LAGP-epoxy hybrid electrolytes (Figure 11e). After undergoing Li plating/stripping, the cycled LAGP pellet was split into several fragments, whereas the structured LAGP-epoxy electrolytes remained in one piece (Figure 11f). From cross-sectional SEM images, a visible detachment of the interphase layer (20–40 µm) from the bulk LAGP phase was observed for the LAGP pellets. In comparison, the structured LAGP-epoxy electrolyte displayed only minor cracks between the bulk electrolyte and interphase layer. When assembled in a symmetrical Li cell, the LAGP-epoxy electrolyte showed more stable voltage polarization at both 0.7 and 1 mA cm$^{-2}$ (Figure 11g). However, the overpotential of the LAGP pellet rapidly reached the limiting voltage of 12 V after 30 cycles. Stress-strain curves from the four-point bending test suggest that the LAGP-epoxy electrolyte had both characteristics of brittle LAGP ceramic and elastic epoxy polymer, as seen in two stress-increasing stages. The epoxy phase maintained superior integrity and made the sample less susceptible to fracture than the ceramic pellet. Therefore, the 3D LAGP-epoxy hybrid solid electrolyte possessed good ionic conductivity and electrochemical stability toward the Li anode, while the overall integrity was significantly strengthened. It should be noted that there is still a long way for the practical application of 3D printing in solid-state batteries due to several challenges. First, 3D printing has special requirements for printing inks, but the available printing ink materials in solid-state batteries are

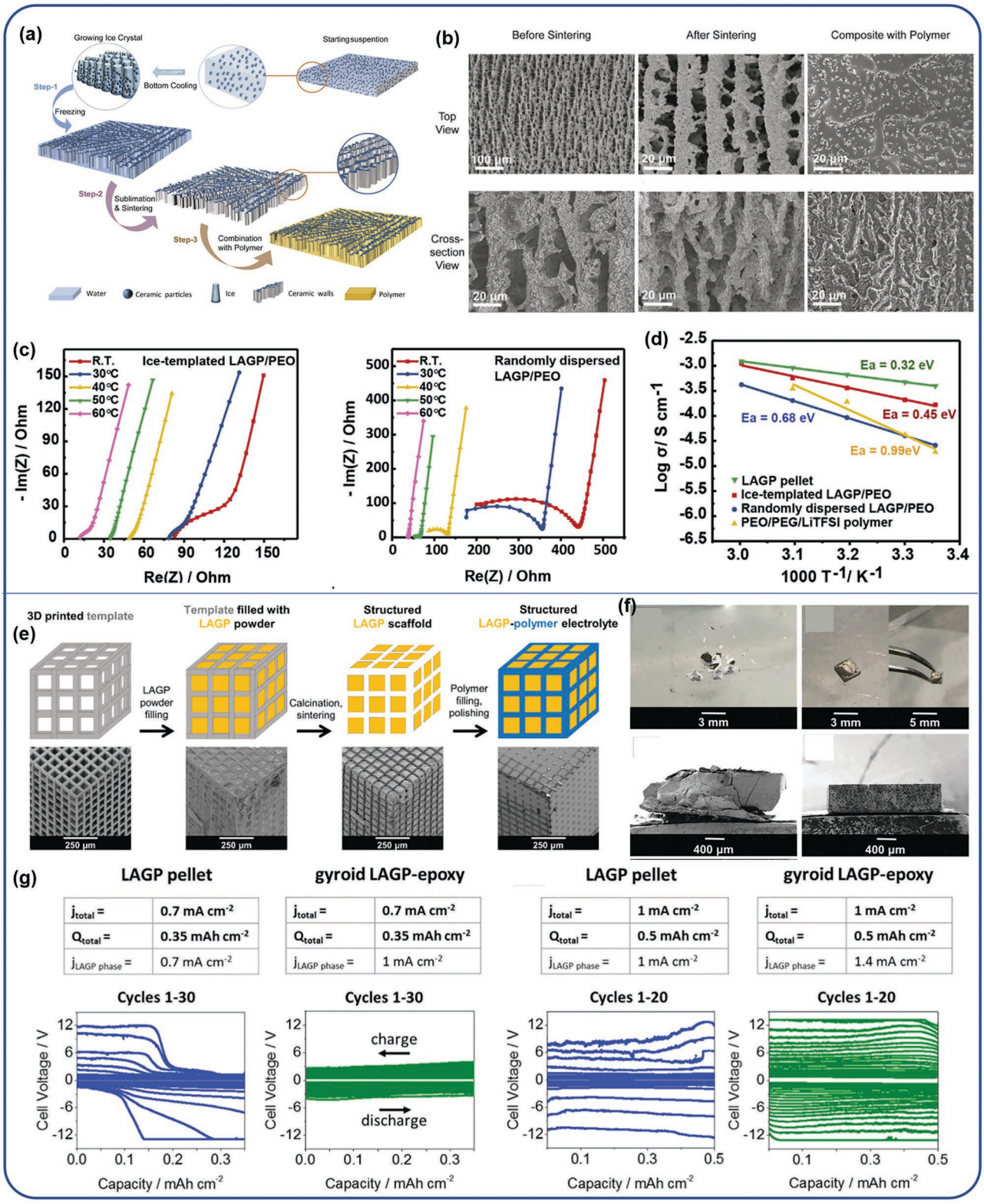


**Figure 11.** a) Schematic of preparation process of LAGP/PEO composite electrolyte by an ice-templating method, b) top view and cross-sectional view of ice-templated LAGP before/after sintering and combining with polymer, c) Nyquist plots of ice-templated and randomly dispersed LAGP/PEO composite electrolyte. d) Arrhenius plots of LAGP pellet, ice-templated LAGP/PEO, randomly dispersed LAGP/PEO and polymer electrolytes. Reproduced with permission.[110] Copyright 2019, Elsevier. e) Schematic of LAGP-epoxy electrolyte by 3D printing and corresponding SEM images, f) post-cycling photos and SEM images of the LAGP pellet and gyroid LAGP-epoxy electrolyte cycled at 1 mA cm$^{-2}$ for 0.5 h per charge and discharge for a total of 20 cycles, g) cycling performance of LAGP pellet and gyroid LAGP-epoxy electrolytes. Reproduced with permission.[113] Copyright 2018, The Royal Society of Chemistry.

yet to be explored more.[114] Second, the post-processing procedures (e.g., carbonization) for hierarchical pores generation by 3D printing are indispensable but time-consuming, which is unfavorable for low-cost manufacturing of 3D printing technology.[115] Additionally, there is still a lack of fundamental investigation about the compatibility of printing ink with high-voltage cathodes or high-capacity cathodes in different battery systems.[116] Thus, replacing conventional solid electrolyte manufacturing with the 3D printing technique is challenging. However, owing to the unique advantage of the arbitrary design of 3D printing, it is worth exploring more advanced 3D printing technologies for customized materials in battery prototyping.

## 5. Conclusions and Outlook

NASICON-type LAGP is a promising solid electrolyte for all-solid-state lithium-ion or beyond Li-ion batteries due to its excellent stability in air and water and good ionic conductivity. However, the further development of LAGP is challenged by the low grain boundary ionic conductivity, poor interfacial compatibility against Li anode or high-voltage cathode, and large thickness prepared by high-temperature sintering. In view of these points, this review summarizes the research progress and advances in the synthesis method, structure modification, and interface design for addressing the Li/LAGP instability issue caused by the reduction reaction of $Ge^{4+}$. The development of LAGP-based solid-state batteries can be accelerated by moving forward in the following aspects.

1) Thin LAGP solid electrolyte films: To compete with liquid-based LIBs, solid electrolytes should have a thickness of ≈20 μm[4a] to achieve high energy density. The conventional pressing and post-sintering method for LAGP synthesis requires high-temperature treatment, increases cost input, and tends to form thick pellets. These large pellets increase internal resistance for Li-ion conduction and eventually drag down the cell-level energy density. On the other hand, thin films are prone to be penetrated by Li dendrites, thus causing an internal short circuit and even safety hazards. It is urgent to develop effective strategies for the preparation of flexible, robust, and thin LAGP solid electrolytes for the commercialization of solid-state batteries. Tape casting, hot pressing, employing polymer or inorganic scaffold, and emerging 3D printing have been reported to achieve LAGP thin films in lab research. The application of these approaches can be extended toward mass production for the commercialization of solid-state batteries.
2) Polymer-LAGP composite solid electrolytes: Polymer-LAGP composite solid electrolytes (CSE) are an effective strategy to combine the advantageous features of both polymer and LAGP. The priority in the following years is to fabricate a cost-effective, easily processible, and robust composite solid electrolyte in order to realize the transition from lab scale to commercialization. The CSE thin film should possess excellent ionic conductivity at room temperature, wide electrochemical window, and good mechanical strength to resist Li dendrites' attack. The study of improving the interfacial stability of CSE toward anode/cathode also deserves more attention and efforts in the future. Specifically, self-healing solid electrolytes or functional layers would be promising in future studies due to their flexibility to accommodate internal/external mechanical change and temperature fluctuation. The reported temperature and stress-resistant solid electrolytes addressed the ionic conductivity loss issue caused by the phase separation that often occurs in traditional composite electrolyte systems.[121] The fast self-healing capacity and environmental adaptability of self-healing electrolytes also stand out in full cell' post-damage capacity recovery under stress or temperature deterioration. More efforts are needed to realize durable and high-energy-density solid-state batteries even under harsh conditions.
3) Interface design of LAGP-based solid electrolytes toward Li anode and high-voltage cathodes: The local chemical potential difference at the cathode-solid electrolyte interface should be reduced to decrease the effect of space-charge layers on Li-ion transport. Rational solid-state cell configuration design requires more studies, for example, introducing an ultrathin buffer layer, or LAGP/electrode integration structure, to resolve the interfacial incompatibility between LAGP and Li anode. Developing effective strategies to ensure intimate contact between LAGP and high-loading cathodes is critical in promoting Li-ion conduction and reducing internal electron transfer resistance. The electrochemical stability of solid electrolytes toward high-voltage cathodes such as NCM requires more effort for high-energy-density ASSLB.
4) Mechanism understanding of LAGP-based solid-solid interfaces: To explore the potential electrochemical reaction, kinetics, and stress change at the solid-solid interface, advanced operando diagnostics are required to reveal the interface chemistry in solid-state batteries, including in situ X-ray diffraction, X-ray photoelectron spectroscopy, nuclear magnetic resonance NMR, electron energy loss spectroscopy, synchrotron radiation, and neutron scattering techniques. In-situ high-resolution transmission electron microscopy is beneficial for observing the dynamic growth of Li dendrites, and the formation of the interphase between anode/cathode and LAGP-based solid electrolytes. Additionally, the integration of theoretical simulations and experimental work will facilitate the in-depth analysis of interfaces in solid-state batteries.
5) Demonstration at pouch cells: Most previous electrochemical testing and cell evaluation for solid-state batteries are based on coin cell data. It is necessary to establish standard pouch cell assembly and testing protocol for a realistic assessment and move forward from lab research to industrial mass production. Extensive efforts are required to solve the potential scientific and technical problems in pouch cells and realize superior energy density at the pouch cell level compared to liquid electrolyte-based LIBs.
6) Battery manufacturing: The manufacturing scalability of solid electrolyte materials should be carefully considered for LAGP-based solid-state batteries. Specifically, the overall cost of LAGP-based SEs highly depends on the availability of raw materials, scaling capacity, and manufacturing processes (e.g., heating, pressing). Compared to the titanium, lanthanum, and zirconium-based oxide compounds LATP, LLZO, and LLTO, LAGP have much higher metal value. One possible solution is to decrease the consumption of Ge in solid

electrolytes (e.g., by partial substitution). On the other hand, price volatility is an essential factor for materials cost evaluation. Ge is produced as a by-product of coal ash and Zn, and its price might be impacted by the supply chain and Ge recycling technology.[122]

7) Safety improvement of LAGP-based solid-state batteries: Li's research group[123] has studied the serious thermal runaway of LAGP against metallic Li at around 300 °C. The accelerating rate calorimeter result and thermodynamic analysis reveal that oxygen generation caused by the heat release and the decomposition of LAGP at the Li/LAGP interface is the origin of thermal runaway. Hence, the applied temperature of solid-state batteries should be carefully chosen and monitored to ensure the safe operation of battery cycling. It is necessary to employ effective strategies to stabilize the Li/LAGP interface and enhance battery safety. Introducing a physical barrier between Li metal and LAGP has been proven feasible in preventing the direct contact of LAGP with Li anode. The rational interface design of solid-state batteries should be considered in further developing LAGP-based solid-state batteries for practical applications.

## Acknowledgements

This work was supported by the Mitacs Accelerate Program, Natural Sciences and Engineering Research Council of Canada (NSERC), Canada Foundation for Innovation (CFI), BC Knowledge Development Fund (BCKDF), the University of British Columbia (UBC), UBCO Eminence Program, Fenix Advanced Materials, and NRC Ideation Fund through New Beginnings Initiative (INB-000654-1). The authors gratefully acknowledge the financial support of the Province of British Columbia through the Ministry of Energy, Mines, and Low Carbon Innovation and the Pacific Institute for Climate Solutions. The authors thank the Office of Energy Research and Development at Natural Resources Canada for financial support. The authors declare that they have no known competing financial interests or personal relationships that could have appeared to influence the work reported in this paper.

## Conflict of Interest

The authors declare no conflict of interest.

## Keywords

all-solid-state lithium-ion batteries, interface engineering, lithium aluminum germanium phosphate, solid electrolytes, thin films

Received: January 27, 2023
Revised: March 7, 2023
Published online: April 28, 2023

[1] a) B. Scrosati, J. Garche, *J. Power Sources* **2010**, *195*, 2419; b) A. Manthiram, *ACS Cent. Sci.* **2017**, *3*, 1063.
[2] a) Z. Yang, J. Zhang, M. C. Kintner-Meyer, X. Lu, D. Choi, J. P. Lemmon, J. Liu, *Chem. Rev.* **2011**, *111*, 3577; b) T. M. Gür, *Energy Environ. Sci.* **2018**, *11*, 2696.
[3] S. Li, S. Q. Zhang, L. Shen, Q. Liu, J. B. Ma, W. Lv, Y. B. He, Q. H. Yang, *Adv. Sci.* **2020**, *7*, 1903088.
[4] a) J. Wu, L. Yuan, W. Zhang, Z. Li, X. Xie, Y. Huang, *Energy Environ. Sci.* **2021**, *14*, 12; b) Y. Pang, J. Pan, J. Yang, S. Zheng, C. Wang, *Electrochem. Energy Rev.* **2021**, *4*, 169.
[5] a) A. Manthiram, X. Yu, S. Wang, *Nat. Rev. Mater.* **2017**, *2*, 16103; b) C. Sun, J. Liu, Y. Gong, D. P. Wilkinson, J. Zhang, *Nano Energy* **2017**, *33*, 363; c) P. Lu, D. Wu, L. Chen, H. Li, F. Wu, *Electrochem. Energy Rev.* **2022**, *5*.
[6] a) J. Dai, C. Yang, C. Wang, G. Pastel, L. Hu, *Adv. Mater.* **2018**, *30*, 1802068; b) S. Lou, F. Zhang, C. Fu, M. Chen, Y. Ma, G. Yin, J. Wang, *Adv. Mater.* **2021**, *33*, 2000721.
[7] X. Yang, K. R. Adair, X. Gao, X. Sun, *Energy Environ. Sci.* **2021**, *14*, 643.
[8] Y. Zheng, Y. Yao, J. Ou, M. Li, D. Luo, H. Dou, Z. Li, K. Amine, A. Yu, Z. Chen, *Chem. Soc. Rev.* **2020**, *49*, 8790.
[9] Z. Gao, H. Sun, L. Fu, F. Ye, Y. Zhang, W. Luo, Y. Huang, *Adv. Mater.* **2018**, *30*, 1870122.
[10] L. Li, Y. Deng, G. Chen, *J. Energy Chem.* **2020**, *50*, 154.
[11] a) S. Abouali, C.-H. Yim, A. Merati, Y. Abu-Lebdeh, V. Thangadurai, *ACS Energy Lett.* **2021**, *6*, 1920; b) W. Lu, M. Xue, C. Zhang, *Energy Storage Mater.* **2021**, *39*, 108.
[12] R. DeWees, H. Wang, *ChemSusChem* **2019**, *12*, 3713.
[13] a) X. Yang, J. Luo, X. Sun, *Chem. Soc. Rev.* **2020**, *49*, 2140; b) F. Zheng, M. Kotobuki, S. Song, M. O. Lai, L. Lu, *J. Power Sources* **2018**, *389*, 198.
[14] E. Umeshbabu, B. Zheng, Y. Yang, *Electrochem. Energy Rev.* **2019**, *2*, 199.
[15] X. Li, J. Liang, J. Luo, C. Wang, X. Li, Q. Sun, R. Li, L. Zhang, R. Yang, S. Lu, H. Huang, X. Sun, *Adv. Mater.* **2019**, *31*, 1808100.
[16] a) J. Lv, R. Zheng, P. Lv, W. Wei, *Energy Environ. Mater.* **2020**, *4*, 208; b) A. Paolella, X. Liu, A. Daali, W. Xu, I. Hwang, S. Savoie, G. Girard, A. G. Nita, A. Perea, H. Demers, W. Zhu, A. Guerfi, A. Vijh, G. Bertoni, G. C. Gazzadi, G. Berti, C. Sun, Y. Ren, K. Zaghib, M. Armand, C. Kim, G. L. Xu, K. Amine, *Adv. Funct. Mater.* **2021**, *31*, 2102765.
[17] W. Zhao, J. Yi, P. He, H. Zhou, *Electrochem. Energy Rev.* **2019**, *2*, 574.
[18] a) J. S. Thokchom, B. Kumar, *J. Power Sources* **2010**, *195*, 2870; b) Y. Zhu, Y. Zhang, L. Lu, *J. Power Sources* **2015**, *290*, 123.
[19] C. R. Mariappan, C. Yada, F. Rosciano, B. Roling, *J. Power Sources* **2011**, *196*, 6456.
[20] M. Zhang, K. Takahashi, N. Imanishi, Y. Takeda, O. Yamamoto, B. Chi, J. Pu, J. Li, *J. Electrochem. Soc.* **2012**, *159*, A1114.
[21] H. Kun, W. Yanhang, Z. Chengkui, Z. Huifeng, L. Yonghua, C. Jiang, H. Bin, M. Juanrong, *Phys. B* **2011**, *406*, 3947.
[22] H. S. Jadhav, M.-S. Cho, R. S. Kalubarme, J.-S. Lee, K.-N. Jung, K.-H. Shin, C.-J. Park, *J. Power Sources* **2013**, *241*, 502.
[23] P. Hartmann, T. Leichtweiss, M. R. Busche, M. Schneider, M. Reich, J. Sann, P. Adelhelm, J. Janek, *J. Phys. Chem. C* **2013**, *117*, 21064.
[24] H. Chung, B. Kang, *Chem. Mater.* **2017**, *29*, 8611.
[25] P. H. Kuo, J. Du, *J. Phys. Chem. C* **2019**, *123*, 27385.
[26] M. Kotobuki, M. Koishi, *Ceram. Int.* **2015**, *41*, 8562.
[27] S. V. Pershina, A. A. Pankratov, E. G. Vovkotrub, B. D. Antonov, *Ionics* **2019**, *25*, 4713.
[28] A. Martinez-Juarez, C. Pecharromán, J. E. Iglesias, J. M. Rojo, *J. Phys. Chem. B* **1998**, *102*, 372.
[29] K. Hayamizu, S. Seki, *Phys. Chem. Chem. Phys.* **2017**, *19*, 23483.
[30] J. Kang, H. Chung, C. Doh, B. Kang, B. Han, *J. Power Sources* **2015**, *293*, 11.
[31] H. Chung, B. Kang, *Solid State Ionics* **2014**, *263*, 125.
[32] S. V. Pershina, B. D. Antonov, A. S. Farlenkov, E. G. Vovkotrub, *J. Alloys Compd.* **2020**, *835*, 155281.
[33] a) M. M. Mahmoud, Y. Cui, M. Rohde, C. Ziebert, G. Link, H. J. Seifert, *Materials* **2016**, *9*, 506; b) B. Yan, L. Kang, M. Kotobuki, F. Wang, X. Huang, X. Song, K. Jiang, *Mater. Technol.* **2018**, *34*, 356.

[34] H. Zhu, J. Liu, *J. Power Sources* **2018**, *391*, 10.
[35] H. Zhu, A. Prasad, S. Doja, L. Bichler, J. Liu, *Nanomaterials* **2019**, *9*, 1086.
[36] G. Yang, D. Safanama, K. C. Phuah, S. Adams, *ACS Omega* **2020**, *5*, 18205.
[37] M. Kotobuki, B. Yan, F. Pan, L. Lu, S. Savilov, S. Aldoshin, *Mater. Today Proc.* **2019**, *17*, 408.
[38] A. Paolella, W. Zhu, G. Bertoni, A. Perea, H. Demers, S. Savoie, G. Girard, N. Delaporte, A. Guerfi, M. Rumpel, H. Lorrmann, G. P. Demopoulos, K. Zaghib, *Adv. Mater. Interfaces* **2020**, *7*, 2000164.
[39] B. Yan, Y. Zhu, F. Pan, J. Liu, L. Lu, *Solid State Ionics* **2015**, *278*, 65.
[40] Y. Zhu, T. Wu, J. Sun, M. Kotobuki, *Solid State Ionics* **2020**, *350*, 115320.
[41] Y. Liu, J. Chen, J. Gao, *Solid State Ionics* **2018**, *318*, 27.
[42] Z. Sun, L. Liu, Y. Lu, G. Shi, J. Li, L. Ma, J. Zhao, H. An, *J. Eur. Ceram. Soc.* **2019**, *39*, 402.
[43] M. Kotobuki, M. Koishi, *J. Asian Ceram. Soc.* **2019**, *7*, 551.
[44] M. Weiss, D. A. Weber, A. Senyshyn, J. Janek, W. G. Zeier, *ACS Appl. Mater. Interfaces* **2018**, *10*, 10935.
[45] S. S. Berbano, J. Guo, H. Guo, M. T. Lanagan, C. A. Randall, *J. Am. Ceram. Soc.* **2017**, *100*, 2123.
[46] S. Wang, J. Wang, J. Liu, H. Song, Y. Liu, P. Wang, P. He, J. Xu, H. Zhou, *J. Mater. Chem. A* **2018**, *6*, 21248.
[47] Y.-C. Kim, K.-N. Jung, J.-W. Lee, M.-S. Park, *Ceram. Int.* **2020**, *46*, 23200.
[48] X. Lu, H. Xiao, *Mater. Lett.* **2016**, *177*, 50.
[49] Y. Nikodimos, L. H. Abrha, H. H. Weldeyohannes, K. N. Shitaw, N. T. Temesgen, B. W. Olbasa, C.-J. Huang, S.-K. Jiang, C.-H. Wang, H.-S. Sheu, S.-H. Wu, W.-N. Su, C.-C. Yang, B. J. Hwang, *J. Mater. Chem. A* **2020**, *8*, 26055.
[50] F. Song, T. Yamamoto, T. Yabutsuka, T. Yao, S. Takai, *J. Alloys Compd.* **2021**, *853*, 157089.
[51] J. S. Thokchom, B. Kumar, *J. Power Sources* **2008**, *185*, 480.
[52] W. Lee, C. K. Lyon, J. H. Seo, R. Lopez-Hallman, Y. Leng, C. Y. Wang, M. A. Hickner, C. A. Randall, E. D. Gomez, *Adv. Funct. Mater.* **2019**, *29*, 1807872.
[53] M. Balaish, J. C. Gonzalez-Rosillo, K. J. Kim, Y. Zhu, Z. D. Hood, J. L. M. Rupp, *Nat. Energy* **2021**, *6*, 227.
[54] Z. Jiang, S. Wang, X. Chen, W. Yang, X. Yao, X. Hu, Q. Han, H. Wang, *Adv. Mater.* **2020**, *32*, 1906221.
[55] M. Zhang, Z. Huang, J. Cheng, O. Yamamoto, N. Imanishi, B. Chi, J. Pu, J. Li, *J. Alloys Compd.* **2014**, *590*, 147.
[56] R. Inada, K.-i. Ishida, M. Tojo, T. Okada, T. Tojo, Y. Sakurai, *Ceram. Int.* **2015**, *41*, 11136.
[57] T. Mousavi, I. Slattery, B. Jagger, J. Liu, S. Speller, C. Grovenor, *Solid State Ionics* **2021**, *364*, 115613.
[58] a) J. Chen, J. Wu, X. Wang, A. A. Zhou, Z. Yang, *Energy Storage Mater.* **2021**, *35*, 70; b) Q. Wang, L. Jiang, Y. Yu, J. Sun, *Nano Energy* **2019**, *55*, 93.
[59] Q. Guo, F. Xu, L. Shen, S. Deng, Z. Wang, M. Li, X. Yao, *Energy Mater. Adv.* **2022**, *2022*, A9753506.
[60] K. Zhang, F. Wu, X. Wang, S. Weng, X. Yang, H. Zhao, R. Guo, Y. Sun, W. Zhao, T. Song, *Adv. Energy Mater.* **2022**, *12*, 2200368.
[61] A. Kubanska, L. Castro, L. Tortet, O. Schäf, M. Dollé, R. Bouchet, *Solid State Ionics* **2014**, *266*, 44.
[62] Z. Sun, L. Liu, B. Yang, Q. Li, B. Wu, J. Zhao, L. Ma, Y. Liu, H. An, *Solid State Ionics* **2020**, *346*, 115224.
[63] K. He, P. Xie, C. Zu, Y. Wang, B. Li, B. Han, M. Z. Rong, M. Q. Zhang, *RSC Adv.* **2019**, *9*, 4157.
[64] A. Paolella, W. Zhu, G. L. Xu, A. La Monaca, S. Savoie, G. Girard, A. Vijh, H. Demers, A. Perea, N. Delaporte, A. Guerfi, X. Liu, Y. Ren, C. J. Sun, J. Lu, K. Amine, K. Zaghib, *Adv. Energy Mater.* **2020**, *10*, 2001497.
[65] E. Ben-Jacob, P. Garik, *Nature* **1990**, *343*, 523.
[66] B. Koohbor, L. Sang, Ö. Ö. Çapraz, A. A. Gewirth, N. R. Sottos, *J. Electrochem. Soc.* **2021**, *168*, 010516.
[67] Y. Liu, C. Li, B. Li, H. Song, Z. Cheng, M. Chen, P. He, H. Zhou, *Adv. Energy Mater.* **2018**, *8*, 1702374.
[68] C. Wang, G. Bai, Y. Yang, X. Liu, H. Shao, *Nano Res.* **2018**, *12*, 217.
[69] Z. Cheng, H. Pan, C. Li, X. Mu, Y. Du, F. Zhang, X. Zhang, P. He, H. Zhou, *J. Mater. Chem. A* **2020**, *8*, 25217.
[70] L. Wang, S. Hu, J. Su, T. Huang, A. Yu, *ACS Appl. Mater. Interfaces* **2019**, *11*, 42715.
[71] S. Xiong, Y. Liu, P. Jankowski, Q. Liu, F. Nitze, K. Xie, J. Song, A. Matic, *Adv. Funct. Mater.* **2020**, *30*, 2001444.
[72] S. Zhang, Z. Zeng, W. Zhai, G. Hou, L. Chen, L. Ci, *Adv. Mater. Interfaces* **2021**, *8*, 2100072.
[73] C. Li, Y. Chen, Z. Li, Y. Zhang, Z. Fang, J. Xu, Y. Sun, H. Bao, H. Cheng, *J. Power Sources* **2021**, *495*, 229765.
[74] Q. Liu, Q. Yu, S. Li, S. Wang, L. Zhang, B. Cai, D. Zhou, B. Li, *Energy Storage Mater.* **2020**, *25*, 613.
[75] C. Ma, Y. Feng, X. Liu, Y. Yang, L. Zhou, L. Chen, C. Yan, W. Wei, *Energy Storage Mater.* **2020**, *32*, 46.
[76] Y. Hu, Y. Zhong, L. Qi, H. Wang, *Nano Res.* **2020**, *13*, 3230.
[77] P. Zhai, L. Fu, S. Yuan, L. Shi, J. Zhu, Y. Zhao, Z. Wang, *ACS Appl. Energy Mater.* **2020**, *3*, 7011.
[78] F. J. Q. Cortes, J. A. Lewis, J. Tippens, T. S. Marchese, M. T. McDowell, *J. Electrochem. Soc.* **2019**, *167*, 050502.
[79] C. Wang, Y. Yang, X. Liu, H. Zhong, H. Xu, Z. Xu, H. Shao, F. Ding, *ACS Appl. Mater. Interfaces* **2017**, *9*, 13694.
[80] Z. Zhang, Y. Shao, B. Lotsch, Y.-S. Hu, H. Li, J. Janek, L. F. Nazar, C.-W. Nan, J. Maier, M. Armand, L. Chen, *Energy Environ. Sci.* **2018**, *11*, 1945.
[81] Z. Cheng, M. Liu, S. Ganapathy, C. Li, Z. Li, X. Zhang, P. He, H. Zhou, M. Wagemaker, *Joule* **2020**, *4*, 1311.
[82] Q. Liu, D. Zhou, D. Shanmukaraj, P. Li, F. Kang, B. Li, M. Armand, G. Wang, *ACS Energy Lett.* **2020**, *5*, 1456.
[83] B. Zhou, D. He, J. Hu, Y. Ye, H. Peng, X. Zhou, X. Xie, Z. Xue, *J. Mater. Chem. A* **2018**, *6*, 11725.
[84] Z. Zhang, S. Chen, X. Yao, P. Cui, J. Duan, W. Luo, Y. Huang, X. Xu, *Energy Storage Mater.* **2020**, *24*, 714.
[85] a) D. Bosubabu, J. Sivaraj, R. Sampathkumar, K. Ramesha, *ACS Appl. Energy Mater.* **2019**, *2*, 4118; b) H. S. Jadhav, R. S. Kalubarme, A. H. Jadhav, J. G. Seo, *Electrochim. Acta* **2016**, *199*, 126; c) W. Li, Q. Wang, J. Jin, Y. Li, M. Wu, Z. Wen, *Energy Storage Mater.* **2019**, *23*, 299; d) D. Safanama, D. Damiano, R. P. Rao, S. Adams, *Solid State Ionics* **2014**, *262*, 211.
[86] C. Zhao, J. Liang, X. Li, N. Holmes, C. Wang, J. Wang, F. Zhao, S. Li, Q. Sun, X. Yang, J. Liang, X. Lin, W. Li, R. Li, S. Zhao, H. Huang, L. Zhang, S. Lu, X. Sun, *Nano Energy* **2020**, *75*, 105036.
[87] Y. Liu, P. He, H. Zhou, *Adv. Energy Mater.* **2018**, *8*, 1701602.
[88] Q. Wang, Y. Lu, J. Jin, C. Chen, Z. Wen, *ChemElectroChem* **2020**, *7*, 4093.
[89] S. Gu, X. Huang, Q. Wang, J. Jin, Q. Wang, Z. Wen, R. Qian, *J. Mater. Chem. A* **2017**, *5*, 13971.
[90] H. Xu, S. Wang, A. Manthiram, *Adv. Energy Mater.* **2018**, *8*, 1800813.
[91] P. Li, X. Li, Y. Guo, C. Li, Y. Hou, H. Cui, R. Zhang, Z. Huang, Y. Zhao, Q. Li, B. Dong, C. Zhi, *Adv. Energy Mater.* **2022**, *12*, 2103648.
[92] Z. Liu, X. Pu, F. Gao, W. Hu, H. Deng, *Energy Storage Mater.* **2019**, *17*, 211.
[93] Z. Cheng, H. Pan, F. Li, C. Duan, H. Liu, H. Zhong, C. Sheng, G. Hou, P. He, H. Zhou, *Nat. Commun.* **2022**, *13*, 125.
[94] L. He, C. Chen, M. Kotobuki, F. Zheng, H. Zhou, L. Lu, *J. Mater. Chem. A* **2019**, *7*, 9748.
[95] E. Zhao, F. Ma, Y. Guo, Y. Jin, *RSC Adv.* **2016**, *6*, 92579.
[96] Z. Zhang, S. Chen, J. Yang, G. Liu, X. Yao, P. Cui, X. Xu, *Electrochim. Acta* **2019**, *297*, 281.

[97] a) T. Ye, L. Li, Y. Zhang, *Adv. Funct. Mater.* **2020**, *30*, 2000077; b) X. Judez, M. Martinez-Ibañez, A. Santiago, M. Armand, H. Zhang, C. Li, *J. Power Sources* **2019**, *438*, 226985; c) L. Chen, Y. Li, S.-P. Li, L.-Z. Fan, C.-W. Nan, J. B. Goodenough, *Nano Energy* **2018**, *46*, 176; d) D. Li, L. Chen, T. Wang, L. Z. Fan, *ACS Appl. Mater. Interfaces* **2018**, *10*, 7069.
[98] J. Lee, T. Howell, M. Rottmayer, J. Boeckl, H. Huang, *J. Electrochem. Soc.* **2019**, *166*, A416.
[99] a) Y. Zhao, Z. Huang, S. Chen, B. Chen, J. Yang, Q. Zhang, F. Ding, Y. Chen, X. Xu, *Solid State Ionics* **2016**, *295*, 65; b) Q. Guo, Y. Han, H. Wang, S. Xiong, Y. Li, S. Liu, K. Xie, *ACS Appl. Mater. Interfaces* **2017**, *9*, 41837; c) G. Hou, X. Ma, Q. Sun, Q. Ai, X. Xu, L. Chen, D. Li, J. Chen, H. Zhong, Y. Li, Z. Xu, P. Si, J. Feng, L. Zhang, F. Ding, L. Ci, *ACS Appl. Mater. Interfaces* **2018**, *10*, 18610.
[100] S. Srivastava, J. L. Schaefer, Z. Yang, Z. Tu, L. A. Archer, *Adv. Mater.* **2014**, *26*, 201.
[101] Q. Liu, Y. Liu, X. Jiao, Z. Song, M. Sadd, X. Xu, A. Matic, S. Xiong, J. Song, *Energy Storage Mater.* **2019**, *23*, 105.
[102] Y.-C. Jung, M.-S. Park, C.-H. Doh, D.-W. Kim, *Electrochim. Acta* **2016**, *218*, 271.
[103] Q. Guo, Y. Han, H. Wang, S. Xiong, W. Sun, C. Zheng, K. Xie, *Electrochim. Acta* **2019**, *296*, 693.
[104] M.-S. Park, Y.-C. Jung, D.-W. Kim, *Solid State Ionics* **2018**, *315*, 65.
[105] Q. Zhang, F. Ding, W. Sun, L. Sang, *RSC Adv.* **2015**, *5*, 65395.
[106] A. Das, M. Goswami, K. Illath, T. G. Ajithkumar, A. Arya, M. Krishnan, *J. Non-Cryst. Solids* **2021**, *558*, 120654.
[107] J. Cheng, G. Hou, Q. Sun, Z. Liang, X. Xu, J. Guo, L. Dai, D. Li, X. Nie, Z. Zeng, P. Si, L. Ci, *Solid State Ionics* **2020**, *345*, 115156.
[108] G. Piana, F. Bella, F. Geobaldo, G. Meligrana, C. Gerbaldi, *J. Energy Storage* **2019**, *26*, 100947.
[109] a) M. C. Gutiérrez, M. L. Ferrer, F. del Monte, *Chem. Mater.* **2008**, *20*, 634; b) S. Deville, E. Saiz, R. K. Nalla, A. P. Tomsia, *Science* **2006**, *311*, 515.
[110] X. Wang, H. Zhai, B. Qie, Q. Cheng, A. Li, J. Borovilas, B. Xu, C. Shi, T. Jin, X. Liao, Y. Li, X. He, S. Du, Y. Fu, M. Dontigny, K. Zaghib, Y. Yang, *Nano Energy* **2019**, *60*, 205.
[111] J. Liu, W. Fang, S. Gao, Y. Chen, S. Chen, C. Hu, S. Cai, Z. Liu, X. Liu, *Mater. Des.* **2020**, *192*, 108753.
[112] W. Zha, W. Li, Y. Ruan, J. Wang, Z. Wen, *Energy Storage Mater.* **2021**, *36*, 171.
[113] S. Zekoll, C. Marriner-Edwards, A. K. O. Hekselman, J. Kasemchainan, C. Kuss, D. E. J. Armstrong, D. Cai, R. J. Wallace, F. H. Richter, J. H. J. Thijssen, P. G. Bruce, *Energy Environ. Sci.* **2018**, *11*, 185.
[114] S. Zhou, I. Usman, Y. Wang, A. Pan, *Energy Storage Mater.* **2021**, *38*, 141.
[115] X. Tian, B. Xu, *Small Methods* **2021**, *5*, 2100877.
[116] D. W. McOwen, S. Xu, Y. Gong, Y. Wen, G. L. Godbey, J. E. Gritton, T. R. Hamann, J. Dai, G. T. Hitz, L. Hu, E. D. Wachsman, *Adv. Mater.* **2018**, *30*, 1707132.
[117] T. Liang, W.-H. Liang, J.-H. Cao, D.-Y. Wu, *ACS Appl. Energy Mater.* **2021**, *4*, 2578.
[118] J. Wang, G. Huang, J.-M. Yan, J.-L. Ma, T. Liu, M.-M. Shi, Y. Yu, M.-M. Zhang, J.-L. Tang, X.-B. Zhang, *Natl. Sci. Rev.* **2021**, *8*, nwaa150.
[119] C. Sun, X. Huang, J. Jin, Y. Lu, Q. Wang, J. Yang, Z. Wen, *J. Power Sources* **2018**, *377*, 36.
[120] N. Shubha, R. Prasanth, H. H. Hng, M. Srinivasan, *J. Power Sources* **2014**, *267*, 48.
[121] W. Lei, X. Jiao, S. Yang, F. B. Ajdari, M. Salavati-Niasari, Y. Feng, J. Yin, G. Ungar, J. Song, *Energy Storage Mater.* **2022**, *49*, 502.
[122] K. J. Huang, G. Ceder, E. A. Olivetti, *Joule* **2021**, *5*, 564.
[123] R. Chen, A. M. Nolan, J. Lu, J. Wang, X. Yu, Y. Mo, L. Chen, X. Huang, H. Li, *Joule* **2020**, *4*, 812.

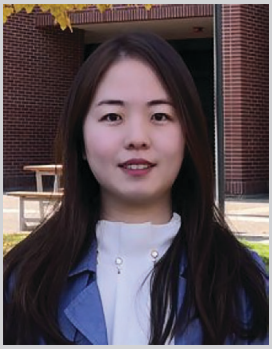

**Yue Zhang** received her Master's degree in engineering from Shanghai Jiao Tong University (SJTU) in 2019. She is currently a Ph.D. candidate under the supervision of Prof. Jian Liu in School of Engineering, the University of British Columbia (UBC) Okanagan campus, Canada. Her research focuses on Te-based next-generation batteries with advanced electrode materials, solid electrolytes, and interface chemistry.

**Jian Liu** is an associate professor and Principal's Research Chair in Energy Storage Technologies at the University of British Columbia (UBC) Okanagan campus, Canada. Dr. Liu received his Ph.D. in materials science (2013) from the University of Western Ontario (Canada) and worked as an NSERC Postdoctoral Fellow at Lawrence Berkeley National Laboratory and Pacific Northwest National Laboratory before joining UBC in January 2017. His current research interests focus on advanced nanofabrication techniques, materials design for Li-ion batteries and beyond, and interfacial control and understanding in energy storage systems.